Study of the anodizing behaviour of additive manufactured AlSi10Mg aluminium alloy

Donovan Verkens

Master thesis submitted under the supervision of
Prof. Iris De Graeve

The co-supervision of
Dr. Reynier Inocente Revilla Castillo

In order to be awarded the Master's Degree in
Chemical and Materials Engineering

Academic year
2016-2017

Contents

Abstract

Study of the anodizing behaviour of additive manufactured AlSi10Mg aluminium alloy (**Donovan Verkens**, **2016-2017**)

Master of Science in Chemical and Materials Engineering: Profile Materials

Selective Laser Melting (SLM) is an additive manufacturing technique that uses a metal powder as a resource to produce near-net-shape parts. In order to do this it uses a high power laser to selectively melt layers of metal powder together. The goal of this thesis is to study the anodizing behaviour of the AlSi10Mg aluminium alloy, to characterise the formed anodic oxide film and to study the effect of the fine microstructure of this material. In this study galvanostatic anodizing was employed in two types of electrolyte, namely: a 3 M sulphuric acid solution and a 0.15 M ammonium tartrate solution. First optical microscopy and Scanning Electron Microscopy (SEM) were used, to characterise the microstructure of the additive manufactured material and to compare it to the microstructure of the AA4420 aluminium cast alloy. Furthermore SEM/EDX (Energy Dispersive X-ray spectroscopy) was also employed to characterise the formed anodic oxide film in the additive manufactured samples and the cast alloy samples. The pores that were formed during galvanostatic anodizing in the sulphuric acid electrolyte solution were studied by using Field Emission - Scanning Electron Microscopy (FE-SEM) and Atomic Force Microscopy (AFM). Finally the corrosion behaviour of the as produced and anodized samples was studied with the help of Open Circuit Potential (OCP) measurements and with anodic polarisation measurements. These corrosion measurements were done in a 0.1 M NaCl electrolyte solution. It was found that for the additive manufactured material the anodizing and corrosion behaviour was depending on the orientation of the considered surface. It was also noticed that the anodizing kinetics of the additive manufactured material was slower than those of the cast alloy material. Furthermore the corrosion resistance of the additive manufactured material was found to be slightly higher than that of the cast alloy material.

Keywords: additive manufacturing, Selective Laser Melting, AlSi10Mg aluminium alloy, galvanostatic anodizing, AA4420 aluminium cast alloy, corrosion

Abstract

Studie van het anodiseergedrag van additief geproduceerd AlSi10Mg aluminium legering (**Donovan Verkens**, **2016-2017**)

Master of Science in Chemical and Materials Engineering: Profile Materials

Selective Laser Melting (SLM) is een additieve productie techniek dat gebruik maakt van een metaal poeder als basis materiaal voor het produceren van bijna volledig gevormde producten. Om dit te kunnen verwezenlijken maakt deze techniek gebruik van een hoogvermogenslaser om zo verschillende metaal poeder lagen aan elkaar te smelten. Het doel van deze thesis is om het anodiseer gedrag van de AlSi10Mg aluminium legering te bestuderen, om de gevormde oxide laag te karakteriseren en om het effect van de fijne microstructuur van dit materiaal te bestuderen. In deze studie werd galvanostatische anodisering toegepast in twee elektrolyten, namelijk: een 3 M zwavel zuur oplossing en een 0.15 M ammonium tartraat oplossing. Eerst werden optische microscopie en Scanning Electron Microscopy (SEM) gebruikt om de microstructuur van het additief geproduceerde materiaal te karakteriseren en om deze te vergelijken met de microstructuur van de AA4420 aluminium gegoten legering. Verder werd ook SEM/EDX (Energy Dispersive X-ray spectroscopy) gebruikt om de gevormde oxide laag in de additief geproduceerde stalen en in de gegoten legeringstalen te karakteriseren. De poriën die werden gevormd gedurende het galvanostatisch anodiseren in het zwavel zuur elektrolyt werden bestudeerd met behulp van Field Emission – Scanning Electron Microscopy (FE-SEM) en Atomic Force Microscopy (AFM). Tenslotte werd het corrosie gedrag van de zoals-geproduceerde en geanodiseerde stalen bestudeerd met behulp van de Open Circuit Potential (OCP) metingen en anodic polarisation metingen. Deze corrosie metingen werden uitgevoerd in een 0.1 M NaCl elektrolyt oplossing. Er werd geconstateerd dat voor het additief geproduceerde materiaal het anodiseer gedrag en het corrosie gedrag afhankelijk is van de oriëntatie van het beschouwde oppervlak. Er werd bovendien ook opgemerkt dat de kinetiek van het anodiseren van additief geproduceerd materiaal trager is dan die van het gegoten legeringsmateriaal. Verder werd er geconstateerd dat de corrosieweerstand van het additief geproduceerde materiaal iets hoger is dan die van het gegoten legeringsmateriaal.

Kernwoorden: additieve productie, Selective Laser Melting, AlSi10Mg aluminium legering, galvanostatisch anodiseren, AA4420 aluminium gegoten legering, corrosie

Abstract

Etude du comportement d'anodisation de l'additif alliage d'aluminium AlSi10Mg fabriqué (**Donovan Verkens**, **2016-2017**)

Master of Science in Chemical and Materials Engineering: Profile Materials

La technique de Selective Laser Melting (SLM) est une technique de fabrication additif par laquelle une poudre métallique est utilisée comme matériau de base pour la production de produits presque entièrement formés. Pour la réalisation de ceci, cette technique utilise un laser haute puissance afin de fondre différentes couches de poudre métallique ensemble. L'objectif de cette thèse est d'étudier le comportement d'anodisation de l'alliage d'aluminium AlSi10Mg, de définir le film d'oxyde anodique façonné et d'étudier l'effet de la microstructure de ces matériaux. Dans cette étude-ci, une anodisation galvanostatique a été utilisée dans deux types d'électrolytes, à savoir un 3 M d' une solution d'acide sulfurique et une solution tartrate d'ammonium 0.15 M. D'abord une microscopie optique et un Scanning Electron Microscopy (SEM) ont été utilisés pour définir la microstructure du matériel additif fabriqué, et pour le comparer avec la microstructure de l'alliage d'aluminium AA4420 coulé. De plus, du SEM/EDX (Energy Dispersive X-ray spectroscopy) fut utilisé pour définir le film d'oxyde anodique formé dans les échantillons additifs fabriqués et dans les échantillons d'alliage d'aluminium. Les pores formés pendant l'anodisation galvanostatique dans l'acide sulfurique électrolyte, ont été étudiés avec le Field Emission – Scanning Electron Microsopy (FE-SEM) et l'Atomic Force Microscopy (AFM). Finalement, le comportement de corrosion des produits fabriqués sans autre traitement et les échantillons anodisés ont été étudiés à l'aide du Open Circuit Potential mesures (OCP) et les mesures de la polarisation anodique. Ces mesures de corrosion ont été effectuées dans une solution de 0.1M NaCI électrolyte. Il fut constaté que pour le matériel additif fabriqué, le comportement d'anodisation et le comportement de corrosion, dépend de l'orientation de la surface considérée. Il fut également constaté que la cinétique de l'anodisation du matériel additif fabriqué est plus lent que celui-ci du matériel d'alliage coulé. De plus il fut constaté que la résistance à la corrosion du matériel additif fabriqué, est légèrement plus élevée que celle du matériel d'alliage coulé.

Mots-clés: fabrication additif, Selective Laser Melting, alliage d'aluminium AlSi10Mg, anodisation galvanostatique, alliage d'aluminium AA4420 coulé, corrosion

Acknowledgement

I would like to express my sincere thanks to:

Professor Iris De Graeve, my supervisor, for giving me the opportunity to do research on this topic and for the guidance and support given during this academic year.

Dr. Reynier Inocente Revilla Castillo, my co-supervisor, for the precious guidance and support given during this academic year.

Bart Lippens for the extensive work done on the preparation of the samples.

Oscar Steenhaut, Kitty Baert, Priya Laha and Marc Raes, for their help and support with the lab equipment and experimental setup.

Introduction

The printing technology was invented around 1439 in Gutenberg, Germany. However the three dimensional printing, also called additive manufacturing, started much later in the 1980s. This additive manufacturing technique produces near-net-shape parts by adding material layer by layer until the final wanted product is obtained. Additive manufacturing has some advantages compared to the conventional production means, like for instance reduced production time, reduction of waste and custom tailoring. Furthermore, additive manufacturing allows for producing more complex parts compared to the conventional production techniques.[1;2]

In the current project the focus is on the 3D printing of aluminium. One type of additive manufacturing techniques is SLM or Selective Laser Melting. The metal alloy of interest is in powder form and a laser is used to selectively melt the metal powder in a designed pattern, which solidifies layer by layer in order to obtain the final three dimensional part.[8]

The materials that are produced with such additive manufacturing technique undergo complex thermal processes resulting in a specific, very fine microstructure, which is very different than in conventional alloy production. The mechanical properties corresponding to this specific type of microstructure and the effect of the SLM process parameters on the microstructure, and indirectly on the mechanical properties, are researched in literature for a small number of alloys. However, there is still a large gap of knowledge to bridge before AM parts can be used for more applications, related to the mechanical properties, but also -and here the number of papers in literature is very low- the surface properties of 3D printed structures, more specifically the corrosion behaviour and corrosion protection of the material.

This thesis is part of a large research project named AEROSTREAM, funded by INNOVIRIS, that studies the applications of additive manufactured aluminium in the aerospace industry. More specifically, the AlSi10Mg aluminium alloy is studied in this project. The mechanical properties of SLM produced material samples are studied (yield strength, ductility, hardness, fatique etc) and related to the microstructure and

process variables by project partners ULB and UCL. The investigation of the surface properties, corrosion behaviour and corrosion protection of these SLM produced AlSi10Mg alloy parts is for the VUB-SURF partner.

For aerospace applications, aluminium is anodized for superior corrosion resistance. This is an electrolytic process which creates a thick stable oxide layer, which is compact or porous depending on the used electrolyte. Porous anodizing is typically performed in an acid electrolyte (mixture). For conventionally produced aluminium, the porous structure and dimensions are closely related to the anodizing voltage/current/time and electrolyte type, concentration and temperature. For conventional aluminium alloys, anodizing is thus well understood and has been used for over 100 years. For AM aluminium however, the anodizing mechanism has not been studied and it is may be quite different due to the totally different microstructure of the AM alloy. Also, the performance of anodized AM aluminium has not been reported in literature.

In this study two different electrolytes will be used. A sulphuric acid electrolyte solution for the formation of a porous oxide layer and a neutral ammonium tartrate electrolyte solution for a barrier type oxide layer. As a reference the AA4420 aluminium cast alloy with similar elemental composition as the AM powder is used to compare its anodizing behaviour to the additive manufactured material. The anodizing response (voltage-time behaviour during galvanostatic anodizing), the oxide layer characteristics (thickness, pore dimensions, growth rate), and the resistance against anodic polarisation (as a first corrosion test) will be compared and evaluated.

Chapter 1

Literature study

1.1 Additive manufacturing

1.1.1 Brief history

The printing industry started already around 1439 in Gutenberg, Germany, and evolved throughout the centuries. Printing of course being limited to 2D at that time.

The modern additive manufacturing started only in the 1980s, when several new technologies were developed that were able to print in three dimensions. The reason why it took the industry so long before it could print in the third dimension is because the associated technologies, like computers, controllers, lasers, etc., that were needed for the process only became available in the 1980s. In the year 1984 several patents were filed in: France, USA and Japan. These patents contained a description of how a three dimensional part can be made, by adding material layer by layer in a selective way. [36]

1.1.2 Advantages

The basic principle of modern additive manufacturing is growing a part layer by layer. As a result, additive manufacturing techniques produce parts which have the dimensions and geometry of the final required part. These near-net-shape parts thus only need a minimum amount of finishing in order to get a finished component. As such production time can be reduced compared to conventional processing. Further, where in conventional products often assembly of components is required, here the piece is printed in one operation, thus simplifying the way the products are made and produc-

ing them in a much more economical way.[13] Also for prototyping AM has proven to be a valuable tool which can be used for various metals and alloys. The produced parts can have virtually unlimited complexity and can be made without the restrictions of conventional machining processes. In other words these processes allow for more design freedom and less waste during production.[1;2]

1.2 Selective Laser Melting

One of the additive manufacturing technologies is selective laser melting or just SLM. The SLM process produces dense metal parts, from three dimensional computer design program data, by using a high power laser to melt and solidify the metal powder layer by layer together. This process allows to obtain a near-net-shape product with much more complex shapes than conventional methods in less time.[1;2]

The first step in the SLM process is to design the required metallic part, this results in a 3D computer aided design (CAD) model. This 3D computer model is then send to the machine's software. In SLM a focused laser beam is used to melt the metallic powder locally and weld different layers of metal powder together in order to get a solid metal part according to the CAD design. The thickness of the metal powder layers depends on the used metal powder, but is in general around 20 micrometres. The setup of the machine consists of the build chamber area with a material dispensing platform, a build platform and a recoating blade, that distributes new powder over the build platform.

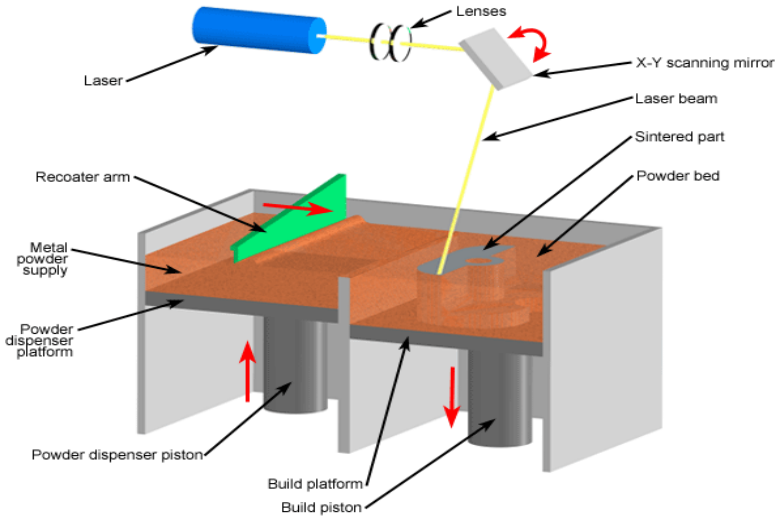

Figure 1.1: SLM machine setup

During the SLM process the laser beam heats and melts the aluminium alloy powder when it scans over this powder layer. The liquid aluminium alloy pool or melt pool that is created then solidifies and the layer starts to form. The moment a layer is finished the building platform lowers, the lowered distance being equal to the powder layer thickness, and the next powder layer is distributed on top of the just finished previous layer and the machine can start to scan again to form the next layer.[8]

1.2.1 Process parameters in additive manufacturing

The SLM process uses generally an Ytterbium fibre laser in order to melt a metal powder in an Ar atmosphere. A great number of process parameters are also involved in the manufacturing process. All these parameters have a considerable influence on the properties of the final part, such as the final density and the surface finish. The hatching process is defined as the movement of the laser beam line after line and this several times. The distance between these lines is constant and is defined as the hatching distance. The powder layer thickness is an important process parameter because it determines in a large extent the density of the obtained part and the cost of the production process. The lower the thickness of the powder layer the higher the density of the final obtained part will be. This is because of the higher extent of interlayer bonding between the different layers. However, the thinner the powder layer the slower the process will be and thus the higher the cost of the operation. Another important parameter is the laser scanning technique that is employed in the process. When a rotation of a certain degrees is employed between these different layers, the overlap between them will be better. This results in more isotropic properties of the obtained final part compared to parts where the layers are built with unidirectional scanning vectors or at least with diagonal scanning vectors.[8;9] Other parameters such as the laser power and the scan speed can also have an influence on the final properties of the manufactured specimen.

1.3 Aluminium in additive manufacturing technologies

Aluminium is a light weight metal with a high strength to weight ratio, a high corrosion resistance and a good formability. All these properties make that aluminium is an excellent material to be used in the transport industry, automotive as well as the aerospace industry. Because of the increasingly interest of using this material in the transport industry the need for new manufacturing technologies, that produce

lightweight metal parts that are close to their final shape and size is only increasing, like the SLM process.[1;2]

Most of the papers in literature are based on the AlSi10Mg alloy.[1;2] However there are a number of other alloys besides pure aluminium, which were also studied in literature. Some of these alloys are Al6061 and AlSi12Mg.[41;42] The interest of these alloys comes from the fact that minor additions of magnesium (0.3 – 0.5 wt%Mg) cause the formation of Mg_2Si precipitates, when the alloy is exposed to a natural or artificial ageing treatment. These precipitates will then cause hardening of the alloy, thus improving the strength properties of the alloy.[47] Furthermore there is also some research done in an other aluminium alloy which was patented by Airbus, namely the ScalmalloyRP0.66-4.5. In this alloy Scandium is the main alloying element under investigation. This alloy has a high strength, a good corrosion resistance and a low density, which makes it a very interesting alloy for the transport industry.[43]

1.4 Characterisation of the AlSi10Mg aluminium alloy used in additive manufacturing

1.4.1 Characterisation of the AlSi10Mg alloy powder

The AlSi10Mg alloy powder is produced by gas atomization and has an approximately spherical shape. This powder has in general an average diameter of about 20 to 40 μm.[48;49;50]

1.4.2 Microstructure of the additive manufactured parts

In this thesis the focus of the research lies on the AlSi10Mg alloy, which is a type of aluminium-silicon alloy. An aluminium-silicon alloy is a binary eutectic system, with a limited solubility of: silicon in aluminium and aluminium in silicon. The solubility of silicon in aluminium reaches a maximum of 1.5 at% at the eutectic temperature. The aluminium-silicon phase diagram, which can be seen in figure 1.2, only shows one invariant reaction:

$$L \rightarrow \alpha + \beta$$

With L being the liquid phase, α the aluminium phase and β the silicon phase. This invariant reaction takes place at the eutectic temperature, 577 °C, and at 12.6 wt% silicon. The additive manufactured material is a hypoeutectic Al-Si alloy, so this

means that the eutectic phase will form in the presence of previously formed primary aluminium.

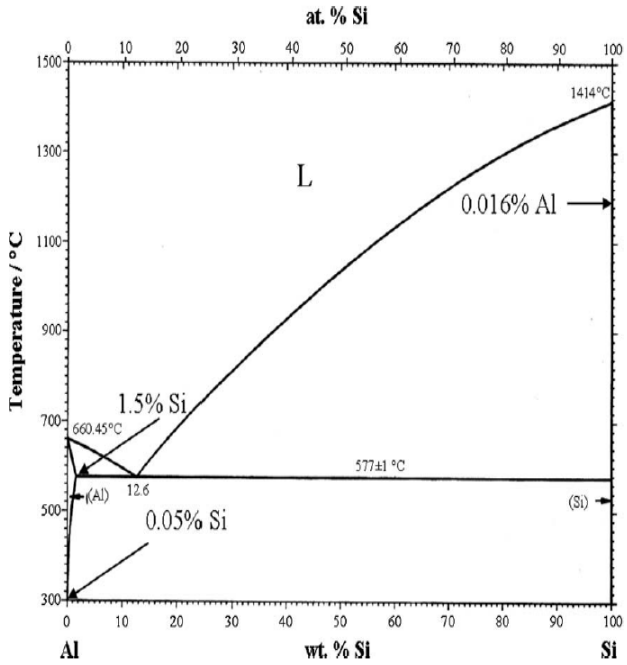

Figure 1.2: Al-Si phase diagram.

However due to very high solidification rates the obtained microstructure of the additive manufactured material will not be determined by the phase diagram, instead a so called 'non-equilibrium' microstructure is obtained.[39]

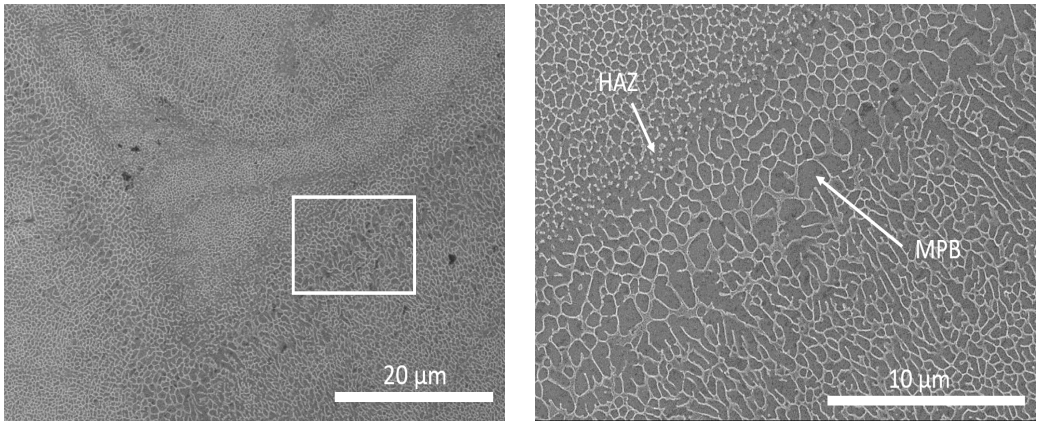

Figure 1.3: SEM image of the microstructure of additive manufactured AlSi10Mg aluminium alloy and a detailed SEM image of a melt pool border (MPB) and heat affected zone (HAZ).[39]

The power of the laser beam and thus the intensity of the laser beam is regulated so that the aluminium alloy powder layer is melted. However also the underlying layer is partially remelted by the laser beam, ensuring a good adhesion between the two layers. Manfredi et al.[8] reported that the melt pools, in a cross section along the building direction of an additive manufactured part, are all oriented in the same direction and that the different layers are superimposed onto each other. The shape of these melt pools cannot be classified as being simply half of a cylinder, because of the partial remelting of the layers and the scanning technique that is being used. And since the shape of the melt pools cannot be classified, their average depth also cannot be determined. Furthermore Manfredi et al.[8] reported that it is reasonable to assume that in a cross section parallel to the building plane the melt pools will originate from different layers. The irregular geometric shapes of the melt pools on this cross section can then be explained by the fact that they can have very different depths and this leads to their contours overlapping.[8]

Olakanmi et al.[34] reported that the assumption can be made that the phase transformation from the liquid state of the melt pool to a solid state required non or almost no free energy to cross the free energy barrier. The absence or almost absence of the free energy barrier is caused by the liquid molten aluminium alloy that allows for a complete wetting of the substrate, and also because of the partially melted grains of the heat affected zone (HAZ), that are located at the fusion boundary, give an almost ideal interface. The HAZ is the region in the layer underneath the current top powder layer that is remelted during the SLM process. The grains are thus formed epitaxially during the solidification. Furthermore the direction of these formed grains is parallel to the local conductive heat transfer.[8]

1.4.3 Mechanical properties of the additive manufactured parts

The high thermal gradients that are intrinsically present in the SLM process cause a lot of residual stresses in the metal part. If these stresses are not relieved the part could get distorted and become dimensionally inaccurate.[3] Furthermore there is a possibility of having cracks and disconnections of components from the building platform. This however can be avoided by heating the building platform.[4] The SLM process causes high temperature gradients in time and space in the metal powder as well as in the different layers of the metal part. The metal powder heats up very rapidly due to absorption of the laser's energy, resulting in melt pools when the melting temperature is exceeded and in heat effected zones in the surrounding metal powder.[5] The greatest disadvantage of SLM however is the fact that the process does not produce a very good surface finish. The laser source produces a metal part with a rough surface, due to droplets and partially melted metal powder on the surface of the part. This rough surface effects the parts fatigue properties and they are altered to such an extent that they cannot be used as such and must undergo a surface treatment.[5]

From previous works in literature[8] it is also known that metal parts, of the AlSi10Mg alloy, that are made by the SLM process have a higher yield and ultimate tensile strength and a higher hardness than the metal parts that were made by conventional means, out of a casting alloy with approximately the same composition. This casting alloy is the A360 aluminium alloy. The higher hardness, yield and ultimate tensile strength of the SLM specimens can be explained by the very fine microstructure and the fine distribution of the silicon phase, which is obtained by extremely rapid cooling and solidification of the specimens. Earlier research reported the possibility of the Mg_2Si intermetallic being present in the SLM specimens on a nanoscale as well as the higher tensile strength of these specimens compared to the A360 casting alloy specimens in the two building directions.[7;8;9;10;11;37]

The mechanical properties of the additive manufactured part can however be altered by means of a heat treatment. The hardness of additive manufactured parts is uniform on a nanoscale, however it is reported in the literature that an adjusted T6 heat treatment results in a lower nano-hardness and in a variation of this hardness in the material. This T6-like heat treatment has the following procedure: first a solution heat treatment is performed for one hour at 520 °C and next an artificial ageing is done for six hours at 160 °C[37] The nano-hardness of the heat treated additive manufactured parts is lower, due to the fact that the finely dispersed silicon, present in the material, will diffuse together in order to form coarser particles. On microlevel, the hardness of the additive manufactured parts showed also a high value, higher than the reference A360 cast alloy. Heat treatment of the additive manufactured material also showed a reduction in hardness on the microlevel, so a softening of the material is reported

for the nanolevel as for the microlevel. This is the opposite what is observed for other conventionally produced Al-Si alloys, they namely harden when exposed to a T6-like heat treatment. This difference in behaviour of the additive manufactured material compared to conventionally produced Al-Si alloys, when exposed to a T6-like heat treatment can be explained by the difference in their microstructure before the heat treatment starts.[37]

The ductility, i.e. the ability to elongate and plastically deform before fracturing, of the additive manufactured material is poor but by employing a T6-like heat treatment it can be increased significantly. So by using this heat treatment: the ductility increases, the yield strength stays at its high level and the ultimate tensile strength only drops in a limited amount.[37]

1.4.4 Corrosion properties of additive manufactured parts

The SLM process produces a rough surface that effects the parts surface properties including corrosion properties. Previous work done in the literature states that the passive protective oxide films of SLM produced aluminium alloys are less protective than naturally formed aluminium oxide films in air.[5] Active behaviour was seen on the surface of SLM specimens during potentiodynamic tests in Harrison's solution, whereas a passive range could be seen for SLM specimens that were polished mechanically and then were allowed to form a natural passive protective film in air.[5]

The porosities present in the SLM produced parts will act as a preferential initiation site for localised corrosion. This localised corrosion was observed at more anodic potentials. In the case of mechanical polished samples localised corrosion was also observed in open porosities where the surface conditions were unchanged and thus the same as the as produced samples. Previous work also revealed that the α-Al phase in the surroundings of the border of the melting pools was dissolved selectively.[6] The effect of shot peening on the corrosion resistance of SLM specimens was also studied in the literature. The shot peening process removes the passive film formed during the SLM process and smoothens the surface of the specimen. Now the passive film is removed a new and better protective oxide layer can form and furthermore the roughness is reduced by one order of magnitude. The biggest disadvantage of this technique is that not all of the passive film can be removed and thus not every area of the surface is protected with the best passive oxide film. Furthermore, it is noticed that shot peened surfaces are not as corrosion resistant as mechanically polished surfaces, however a better corrosion resistance compared to as produced surfaces is noticed.[6;2]

Since studies in the literature point out that the protection of the passive oxide layer of SLM specimens against corrosion is not as good as the protective power of the

oxide layer of conventional produced specimens, it is clear that finding a good surface treatment for these SLM manufactured parts, so that their resistance to corrosion and the quality of the passive oxide layer increases, becomes very important. The chromate based surface treatments are very effective, but are no longer used because studies revealed that Cr(VI) is very toxic.[12] That is why a lot of research is done for finding a good alternative process for these chromate based treatments. Some of the more promising surface treatments are bright dipping, which is a process that uses a bath containing mostly phosphoric and nitric acid to reduce the roughness of the surface, and Ce(III) conversion treatment. It was observed that the bright dipping technique improved the corrosion resistance of as produced SLM specimens, because it removed the less protective passive film. On the other hand it reduced the corrosion resistance of mechanically polished SLM specimens, because the etching of the surface induces silicon enrichment. The Ce(III) conversion treatment was proven not to be effective on as produced SLM specimens even when it was combined with bright dipping. This is because of the defects on the surface of these specimens that will prevent the Ce to deposit in the porosities and prevent the forming of a continuous compact film. However, the Ce(III) conversion treatment was effective on mechanically polished and bright dipped SLM specimens, with the treatment's effect more noticeable on the plane perpendicular to the building plane.[2]

In aerospace applications, a common surface treatment of aluminium alloys to improve the corrosion resistance as well as the bonding with overlying paint coatings, is however anodizing. This process has not been reported for SLM aluminium in literature and hence should be investigated.

1.5 Anodizing of aluminium and aluminium alloys

1.5.1 Oxide growth mechanism and the effect of process variables

Anodizing is an electrolytic process where aluminium is oxidized in a specific electrolyte to form a stable compact or porous oxide layer, depending on the type of electrolyte. Anodizing can be performed under potentiostatic or galvanostatic control, using AC or DC current. In all situations, the mechanism involves the high-field migration and combination of oxygen anions from the electrolyte and aluminium cations (aluminium is anodically polarised) across the (pre)existing and growing oxide film. Under galvanostatic control a constant current – the operating mode which will be used in the current project- is applied between working and counter electrode and the anodizing potential can be monitored, giving insight into the oxide formation mechanism as illustrated in

Figure 1.4. Figure 1.4 represents two types of anodizing behaviour, showing the anodizing potential as a function of processing time of pure aluminium galvanostatically anodized in (curve A) an acid electrolyte, such as sulphuric acid, and in (curve B) a neutral electrolyte, such as ammonium tartrate.

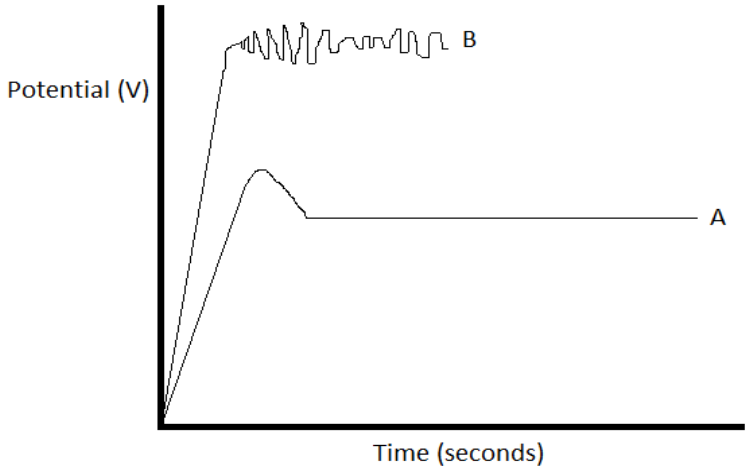

Figure 1.4: Dependence of the anodizing potential on anodizing time for galvanostatic anodizing of pure aluminium at constant current density, in a neutral anodizing electrolyte (B) and in an acid anodizing electrolyte solution (A) at constant temperature and concentration. (theoretical curves to explain the oxide formation mechanism)

As can be seen in figure 1.4 anodizing curve B shows a first part where the voltage increases linearly with time, followed by an oscillating region. Curve B represents a typical barrier oxide growth in neutral electrolyte solution: in the linear part the thickness of the oxide layer increases with time until the moment of electrical breakdown (around 1000 V for alumina) where the anodizing potential starts oscillating in time.[16] This barrier oxide is formed by migration of O^{2-} ions coming from the aqueous electrolyte, due to the imposed electric field, in the direction of the bulk material across the pre-existing oxide layer to the oxide/metal interface where it will react with the aluminium cations.[17;18;19;20]

Curve A in figure 1.4 shows first again a linear increase of potential in time, followed by a potential drop (typical for pure aluminium; less present for aluminium alloys) to reach an approximately constant value with further anodizing process time. This type of anodizing curve is characteristic for combined barrier/porous oxide growth. The oxide layer thickens relatively uniformly as a function of time in the steady state region of the anodizing curve and the major anodic oxide dimensions (barrier layer,

pore dimensions) are determined by the potential corresponding to this steady state.[17] The rate of increase of the potential in the linear part is depending on the used anodizing solution as is the potential maximum and the potential value of the steady state region.[21] The linear increase in potential in the beginning of curves A and B corresponds to the formation of the barrier oxide and the higher the slope the higher the rate of barrier oxide layer formation. However, curve A shows that after the linear part and a maximum value of potential is passed, the potential drops till a constant value is reached and maintained. This drop in potential can be explained by the fact that during this phase in the anodizing process the thickness of the barrier oxide layer declines due to the nucleation of pores at the outer surface of the barrier oxide layer, due to the destabilizing effect of the acid electrolyte. After the nucleation of the pores, a self-organising mechanism driven by the electric field across the oxide, results in a regular distribution of pores (in a regular hexagonal close-packed pattern). The porous oxide layer grows simultaneous with the dissolution/formation of the barrier oxide layer at the pore bases. This results from the migration of O^{2-} ions in the direction of the bulk material to the metal/oxide interface where they will react with the oxidized aluminium, and the simultaneous electrical field assisted migration of Al^{3+} ions through the oxide layer in the outward direction. These outward moving Al^{3+} ions are ejected from the pore base into the acid electrolyte and will not form a solid oxide.[22] That is why an approximately constant potential is observed in the steady state region of the anodizing curve, where there exists a dynamic equilibrium between oxide formation and oxide dissolution at the pore base, while the pores elongate and the oxide/metal interface regresses into the substrate. This results in a constant thickening of the porous layer section.

Increasing the anodizing current density speeds up the oxide growth process.[16] The faster the process, however, also the faster the temperature of the bath can rise due to Joule heating. When this effect becomes the predominant factor it will promote the chemical dissolution process of the barrier oxide layer.[21] Another effect of these high current densities is that not only the temperature of the bulk electrolyte in the bath will increase but also the temperature of the electrolyte in the pores of the oxide layer, even with intense stirring. A direct consequence of this effect is the decrease of the potential in the steady state regime.[23;24] In extreme cases this can lead to burning of the oxide, which is a local breakdown of the layer and of course deterioration of the oxide properties.

The concentration of the electrolyte influences this growth mechanism.[16] At higher concentrations the chemical dissolution of the oxide becomes more pronounced in the anodizing mechanism; at too high concentrations oxide dissolution can predominate resulting in an excessive dissolution both at the pore bases and at the outer surface of the growing oxide leading to truncated pores and a general decrease of oxide layer

thickness.[25]

As for higher concentrations of the acid electrolyte, also higher temperatures promote the oxide dissolution at the pore base and the pore walls and as a result the pore diameter increases. A common behaviour for most acid electrolyte solutions is that, the higher the anodizing temperature the lower the slope of the linear part of the anodizing curve will be and thus the lower the rate of barrier oxide formation.[21;25]

1.5.2 Pores in the porous oxide layer

Literature predicts the dimensions of the formed pores in the combined barrier/porous oxide layer. It is reported that the pore cell diameter (in nm) is about 2.5 to 2.7 times the reached anodizing potential (in Volt). The barrier oxide layer thickness d (in nm) is predicted to be 1.0 to 1.2 times the reached anodizing potential (in Volt). Furthermore, the pore diameter p (in nm) is than calculated to be 1.3 to 1.7 times the reached anodizing potential (in Volt).[40]

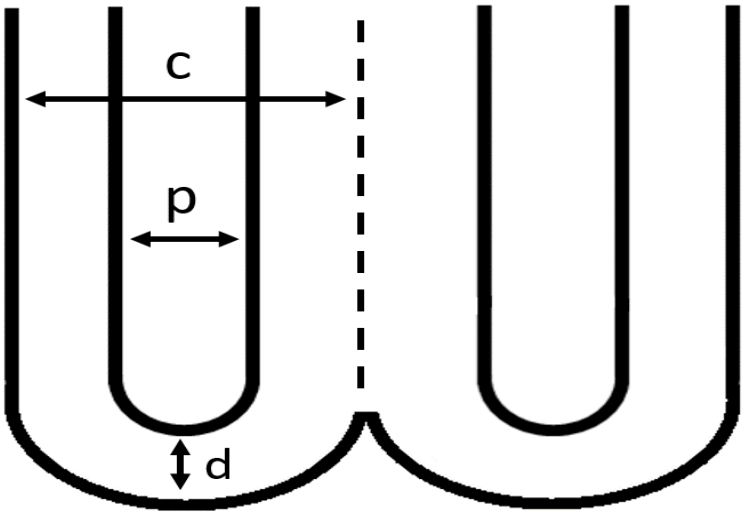

Figure 1.5: Schematic image of the dimensions of the formed pores in the porous oxide layer, with d = 1 - 1.2 nm/V, p = 1.3 - 1.7 nm/V and c = 2.5 - 2.7 nm/V, this potential (V) is the final reached anodizing potential.[40]

1.5.3 Anodizing of silicon-aluminium cast alloys

1.5.3.1 Influence of silicon

When a silicon-aluminium cast alloy is anodized, the formed oxide layer will contain silicon particles. This is because the silicon is not dissolved or anodized at the same rate as the aluminium. When the moving oxide front - at the metal/oxide interface regressing into the metal bulk - meets a silicon particle the oxide growth direction changes and moves around the silicon phase and thus embeds it in the growing oxide layer.[27] But these embedded silicon particles are at the same time partially anodized, resulting in the formation of a silicon oxide film that covers the particles. The anodizing of silicon is made possible by it's semiconducting properties, that allow, the for anodizing necessary, field-assisted transport of ions in the oxide layer.[44] A thickness of about 40 nm is observed in literature for this film.[26]

Further, it is observed in literature that the anodizing of cast alloys with silicon particles results in the formation of cracks and cavities above the silicon particles, during the anodizing process. It appears that the oxidation of the silicon particles is responsible for this.[26;28] The cracks and cavities could form as a result of a stress relieving mechanism. The volume expansion around the particles, due to the oxidation of the silicon, results in the creation of this intrinsic localised stress, that is the source for the cavities and cracks. On the other hand for materials where the silicon particles have been modified, with the introduction of Sr to the material, less cavities and cracks are observed around the silicon particles.[27] This suggests that the morphology of the silicon particles - which have changed from flake-like interconnected particles into fibrous disconnected particles due to addition of Sr - has an effect on the amount of cavities and cracks present in the material. Smaller fibrous silicon particles, which are less interconnected, accumulate less stress and thus generate a lower amount of cavities and cracks around the silicon particles.[27] This change in morphology appears to also have an effect on the formed silicon oxide film, the modified silicon particles will be anodized to a higher extend than the unmodified particles.[26]

So when the regressing aluminium oxide front meets a silicon particle it will move around this particle, because the anodizing of the silicon phase into a silicon oxide film is much slower. The amount of silicon oxide formed for a silicon particle is determined by the size of this particle and the morphology or more specifically the interconnection of this particle with the other silicon particles. The silicon oxide film is mostly found on the side of the particle that faces the moving oxide front. The anodization of the silicon particle is however stopped when the oxide front moves around the silicon particle, embedding it in the aluminium oxide layer and leaving it only partially oxidised and isolated from the bulk material. The silicon particles can, depending on their shape,

also prevent the oxidation of some of the aluminium phase underneath it. The silicon particle does this by shielding the aluminium from the moving oxide front, as such preventing it from anodizing. The oxide front then moves on and embeds the partially oxidised silicon particle and the aluminium phase in the aluminium oxide layer. This is illustrated in the schematic figure below. This unanodized aluminium phase is most often found between and under the embedded silicon particles in the oxide layer.[27]

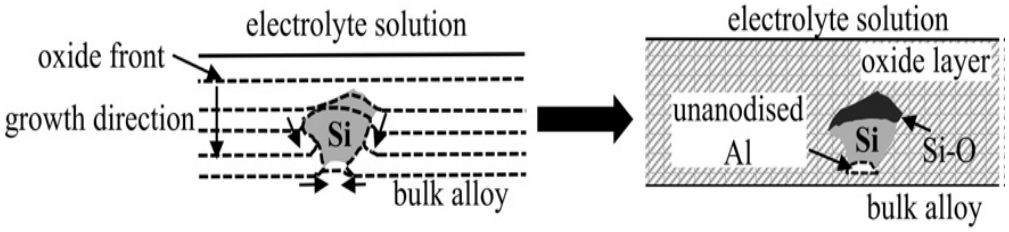

Figure 1.6: The behaviour of the silicon particles during the anodizing process.[27]

1.5.3.2 Influence of the eutectic phase morphology

1.5.3.2.1 Size and shape of the silicon particles

The eutectic phase contains most of the silicon particles and the Mg_2Si intermetallic of the silicon-aluminium cast alloy, as well as some aluminium phases. As a result, because of the presence of these silicon particles, the oxide front moves at a lower rate and in an inhomogeneous fashion through the eutectic phase, in comparison with the rate at which the oxide front moves through the aluminium phase. Because of these different anodization rates the growth direction of the oxide front will move from the aluminium phase towards the eutectic phase.[27]

When Sr is introduced into the cast alloy material the polygonal flakes of silicon particles, that are interconnected to form a three dimensional network, change in morphology. And, as mentioned earlier, they change into fibrous particles that are not interconnected. This modification of morphology will affect the growth kinetics of the oxide layer. When the silicon particles are unmodified the oxide front moves through the aluminium phase in the eutectic phase and moves around the flake-like silicon particles. Because of the morphology of these unmodified silicon particles, being large and interconnected, the space between the polygonal flakes is narrow and thus a large portion of the aluminium phase is shielded from the moving oxide front.[29] As a result of this a large amount of quite large unanodized aluminium inclusions are present in the formed oxide layer, as is represented in figure 1.7.[27]

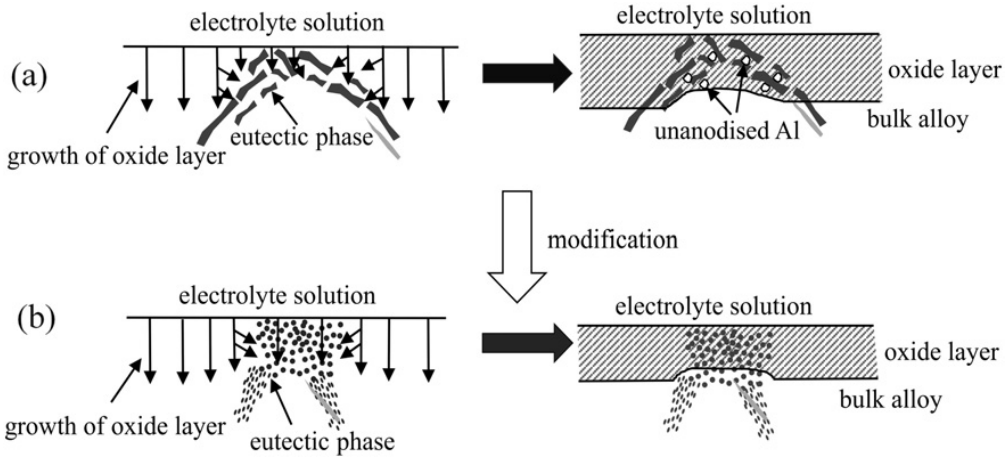

Figure 1.7: The effect of the eutectic phase on the growth kinetics of the oxide layer, with the cast alloy in unmodified conditions (a) and in modified conditions (b).[27]

On the other hand when the silicon particles are smaller (modified due to addition of Sr, for example) and are not connected in a three dimensional network, the oxide front moves more easily and in a more homogeneous fashion through the aluminium phase in between the silicon particles. This less obstructed movement of the oxide front results in a smaller amount of unanodized aluminium in comparison to the cast alloy with unmodified silicon particles. If some unanodized aluminium still remains, it can then be found underneath some of the silicon particles, with their dimensions being at the nanometer scale. Furthermore the oxide front also reacts with the smaller silicon fibres and as a result a relatively high amount of silicon oxide film is being formed.[27]

1.5.3.2.2 Size and shape of the silicon eutectic phase distribution

The cooling rate, that was used in the production of the cast alloy material, will have a significant effect on the morphology of the eutectic phase of the material. And like discussed earlier, the morphology of the eutectic phase will have an effect on the oxide growth. The higher the cooling rate the more refined the aluminium phase and the larger the eutectic phase will be. When on the other hand a lower cooling rate is used the aluminium phase will be larger and consequently the eutectic phase will be smaller. When the eutectic phase is smaller the chance of it ending up in the formed oxide layer becomes smaller. The cooling rate can also have another effect on the oxide growth kinetics, because the higher the cooling rate the less pure the aluminium phase will be. This aluminium phase of lesser purity contains more silicon particles because there was less time for solid state diffusion. The lower the cooling rate the more solid state diffusion can occur and thus the lower the amount of silicon present

in the aluminium phase . This results in a thicker oxide layer, since there is less silicon present to obstruct the moving oxide front. The effect of the cooling rate is represented in figure 1.8.[27;30;31;32]

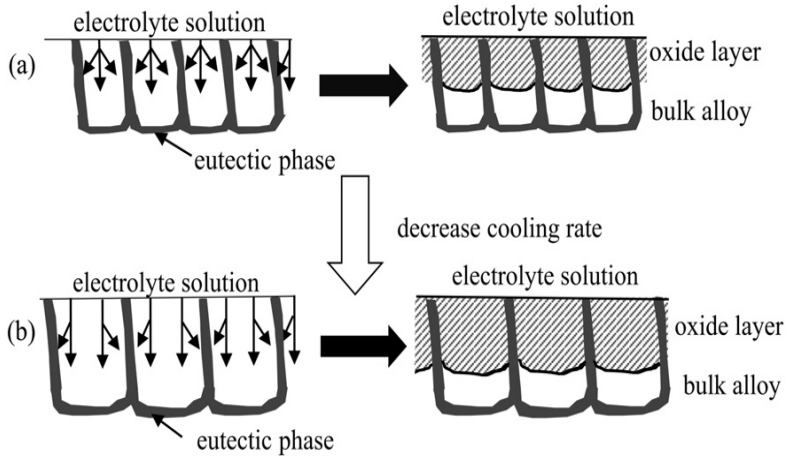

Figure 1.8: The effect of the cooling rate on the oxide growth kinetics, in case of a high cooling rate (a) and in case of a low cooling rate (b).[27]

1.5.3.2.3 Influence of the silicon phase concentration

A silicon-aluminium cast alloy with a low concentration of silicon has a small eutectic phase that has either a thin or a broken structure. A high concentration cast alloy on the other hand has a larger eutectic phase and a more refined aluminium phase. It appears now that by increasing the silicon concentration in the cast alloy the resulting oxide layer, formed by anodization, will be less thick. Moreover the higher the silicon concentration the more silicon particles that will be embedded during the anodization.[27;28] The observation that the formed oxide layer will be less thick in case of a higher silicon concentration cast alloy, can be explained by the fact that the oxide front moves at a slower rate through the eutectic phase, which contains most of the silicon particles. When the oxide front moves through a cast alloy with a high amount of eutectic phase there will be a high probability that the oxide front will stumble upon this eutectic phase and will have to move through is at a slower rate. This results in a oxide layer with a lower thickness and the distribution of its thickness is less uniform. This is represented in figure 1.9.[27]

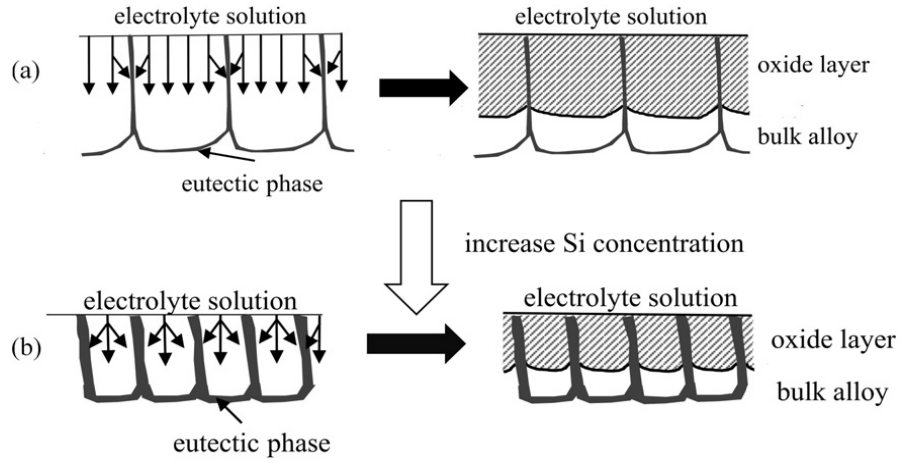

Figure 1.9: The effect of the concentration of the silicon phase on the oxide growth kinetics, in case of a low concentration of silicon (a) and in case of a high concentration of silicon (b).[27]

1.6 Techniques

1.6.1 Scanning Electron Microscopy and Energy Dispersive X-ray spectroscopy

Scanning Electron Microscopy (SEM) is a type of microscopy that makes topography and compositional contrast images of a sample by scanning the surface in a raster pattern with a focused beam of electrons. The incident electrons interact with the atoms in the sample producing: secondary electrons that will be used for topographical images and backscattered electrons that will be used for compositional contrast images. SEM can have a resolution better than 1 nm. Further, it is possible to measure a sample in a high vacuum, a low vacuum, in situ and at a wide range of temperatures in certain setups. The incident electrons furthermore also produce x-rays, characteristic to the atoms of the sample, that will be analysed in Energy Dispersive X-ray spectroscopy (EDX) to make an elemental mapping of the sample.[45]

1.6.2 Atomic Force Microscopy

AFM or Atomic Force Microscopy is a kind of scanning probe microscopy, that has atomic resolution. The information about a sample is gathered by the movement of a mechanical probe over the sample's surface. The principle of AFM is based on the

finite interaction forces between the atoms of the surface of the sample and the atoms of the tip of the mechanical probe. As a result of these forces the tip and cantilever of the probe will move up or down. As a result of this movement of the probe the laser beam will be reflected differently onto the photodiode, which then will register another height. This allows for the determination of the topography of the sample's surface along with the measurement of the forces between the sample and the tip of the probe. AFM is able to form a 3D image of the sample's surface with, in principle, an atomic resolution. AFM has three modes, namely: contact mode, non-contact mode and tapping mode. The movement of the probe on command is than accommodated by tiny piezoelectric components on the probe.[46]

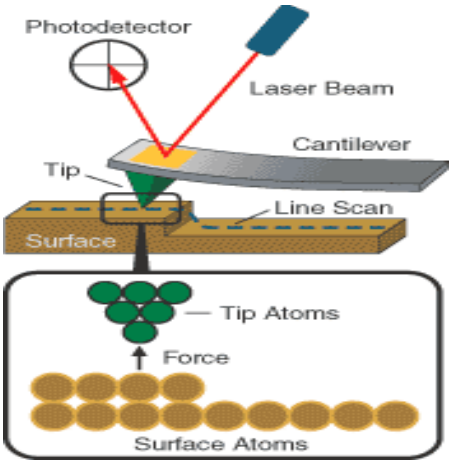

Figure 1.10: Principle of AFM

1.6.3 Linear Sweep Voltammetry

Linear Sweep Voltammetry (LSV) is a voltammetric method that measures the current between the working electrode (WE), which is the metal sample, and the counter electrode (CE) as a response to the applied linearly increasing potential in time between the working electrode and the reference electrode (RE). This three electrode configuration is used a lot in electrochemical measurements.

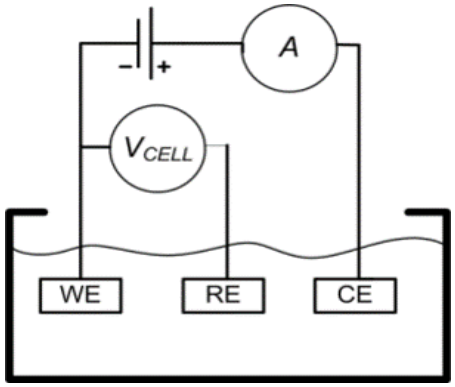

Figure 1.11: Three electrode configuration for electrochemical measurements.

A plot of the measured current as a function of the applied voltage represents the electrochemical behaviour of the metal sample. The recorded current peaks in this plot represent the oxidation or reduction reactions of the species in the metal sample. This measuring method is used frequently in electrochemistry for corrosion experiments like measuring of the corrosion rate and passivity of metal alloys.[45]

1.6.4 Open Circuit Potential

The Open Circuit Potential (OCP) of a metal sample in an aqueous solution is a function of the reactivity of this metal, the electrolyte and the experimental conditions. This OCP is measured with respect to a reference electrode such that a change in potential is only caused by a change in potential at the metal/electrolyte interface.[45]

Chapter 2

Experimental conditions

2.1 Samples

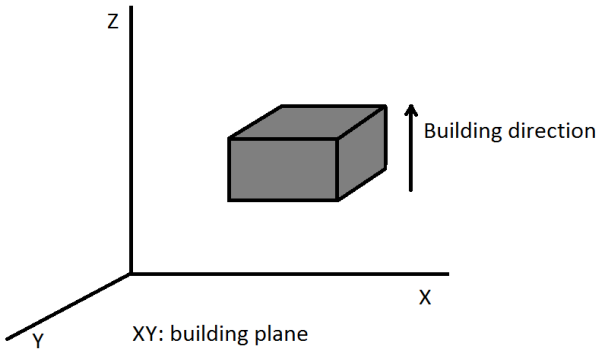

Figure 2.1: Additive manufactured sample, with the Z-direction being the building direction and the XY plane being the building plane.

Figure 2.1 shows how in the next sections the AM samples are labelled according to the plane of investigation, with the Z direction as building direction and the XY plane the building plane. The samples will be labelled AMXY and AMXZ. AMXY is a sample with the studied plane being in the XY plane and AMXZ is a sample with the studied plane being in the XZ plane. The process parameters by which these samples were produced are proprietary information of Layerwise-3D systems. The chemical composition of this AM material is determined by EDX and can be seen in the table below.

(wt%)	Cu	Fe	Mg	Mn	Si	Zn	Al
AM AlSi10Mg	/	0.11	0.34	0.01	9.55	/	balance

Table 2.1: Chemical composition of the AM AlSi10Mg alloy in wt%.

The AA4420 aluminium cast alloy, which has a comparable chemical composition to the AM material, is taken in this thesis as a reference sample, labelled CA. With thanks to Aleris Duffel who provided this cast alloy. The chemical composition of this material is shown in the table below.

(wt%)	Cu	Fe	Mg	Mn	Si	Zn	Al
AA4420	0.07	0.38	0.5-0.7	0.09	9.48-9.89	0.18	balance

Table 2.2: Chemical composition of the silicon-aluminium cast alloy in wt%.

2.2 Anodizing procedure

The samples are prepared by embedding the AM part in an epoxy resin, with on one side of the AM part an electrical connection with a copper wire. The exposed surface of the AM part is then mechanically ground and polished, finishing with 0.04 μm standard colloidal silica suspension (OP-S). Next the samples were cleaned ultrasonically in acetone and ethanol for 3 minutes each. The samples were then rinsed with ethanol and deionised water. And finally the samples were dried under a cool air stream.

The anodizing was carried out, with a Delta Elektronika Power Supply ES 0300-0.45, in a stirred electrolyte solution galvanostatically at 10mA/cm^2 and at room temperature, while measuring the anodizing potential as a function of the anodizing time. The anodizing was done by using a two electrode cell, with a round platinum counter electrode that has a surface area of 7.07 cm^2, in the following two electrolytes:

- 3 M H_2SO_4
- 0.15 M Ammonium tartrate

After anodizing the samples were washed with distilled water and dried with a cool air stream.

2.3 Optical microscopy

Optical microscopy was used to characterise the microstructure of the samples, and to study the formed oxide layer on both the AM material and the cast alloy. A Leitz Metallovert optical microscope was used.

2.4 Scanning Electron Microscopy

Scanning Electron Microscopy (SEM) and Energy Dispersive X-ray spectroscopy (EDX) were used to characterise the microstructure of the samples, and to study in detail the formed oxide layer. The used SEM/EDX was a JEOL JSM-IT300 with a 15 kV acceleration voltage, a 8 pA probe current and a working distance of 10 mm.

Field Emission - Scanning Electron Microscopy (FE-SEM) was used to have a better understanding of the formed pores in the oxide layer, using the sulfuric acid solution as the electrolyte, and to further study the microstructure of the samples. In order to be able to characterise the microstructure, the samples were etched with Keller's etchant. The FE-SEM was a JEOL JSM-7100F with a 15 kV acceleration voltage, a 8 pA probe current and a working distance of 10 mm.

2.5 Atomic Force Microscopy

AFM measurements were performed with a Park Systems XE-100 atomic force microscope in ambient conditions. In these measurements a rectangular conductive cantilever (ANSCM–PT fromAppNano) was used that has: a Pt/Ir coating, a resonant frequency of 50 - 70 kHz and a spring constant of 1 - 5 N/m. A scanning rate of 0.2 Hz was employed during topographic measurements. The topographic measurements were performed in a dynamic mode and with a single pass methodology. This technique was employed to study the pore dimensions of porous anodized AM and cast alloy samples in cross-section.

2.6 Potentiodynamic polarisation

Electrochemical measurements like OCP determination and anodic polarisation were used to study the corrosion properties of polished AM material and aluminium-silicon

cast alloy, before and after galvanostatic anodizing in sulphuric acid electrolyte. Specific anodizing times of 1200 and 724 sec for the AM and the cast alloy respectively were chosen such that the thickness of the oxide layer is about 4 μm for both materials. The OCP measurements and the anodic polarisation experiments were done by using an AUTOLAB Potentiostat-Galvanostat PGSTAT 30. The experimental setup consists out of a three electrode configuration, where the sample is the working electrode, a platinum electrode acts as the counter electrode and a saturated Ag/AgCl (210 $\pm$ 15 mV vs SHE) electrode is used as the reference electrode. These experiments were carried out at room temperature in an 0.1 M NaCl electrolyte solution. First the OCP was determined during 2 hours, after immersion of the sample in the electrolyte, with a measuring interval of 0.1 seconds. Next the anodic polarisation experiment started at 10 mV below the OCP until 1.6 V above the OCP, a scanning rate of 0.1 V/min and an automatic current range between 10 nA and 1 A was chosen. These experiments were done three times for each sample.

Chapter 3

Results and discussion

3.1 Microstructure

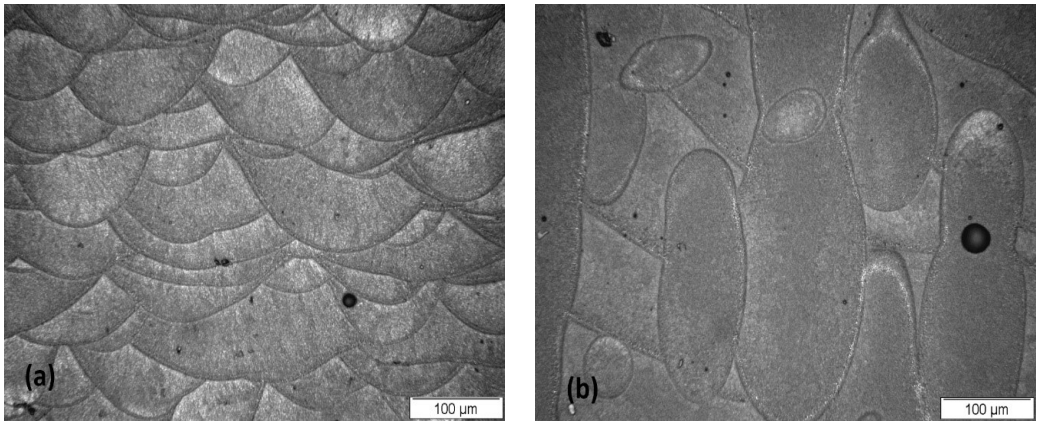

Figure 3.1: Optical microscopy images of an AM part, in the XZ plane (a) and in the XY plane (b).

Figure 3.1 shows the images, made with optical microscopy, of the microstructure of an AM part: in the XZ plane (a) and in the XY plane (b). Figure 3.1(a) shows that the melt pools are oriented in the same direction, that the different layers of the part are superimposed onto each other and that the shape of the melt pools cannot be defined as being simply half cylindrical because of the partial remelting of layers and the scanning technique, as was also reported by Manfredi et al.[8] Figure 3.1 (b) shows the irregular shaped contours of the melt pools in the XY plane, which is also reported

by Manfredi et al.[8]

This results from the fact that the melt pools can have a wide range of possible depths which leads inevitably to their contours overlapping. Furthermore figure 3.1 also shows that the amount of melt pool borders per surface area is larger in the XZ plane than in the XY plane.

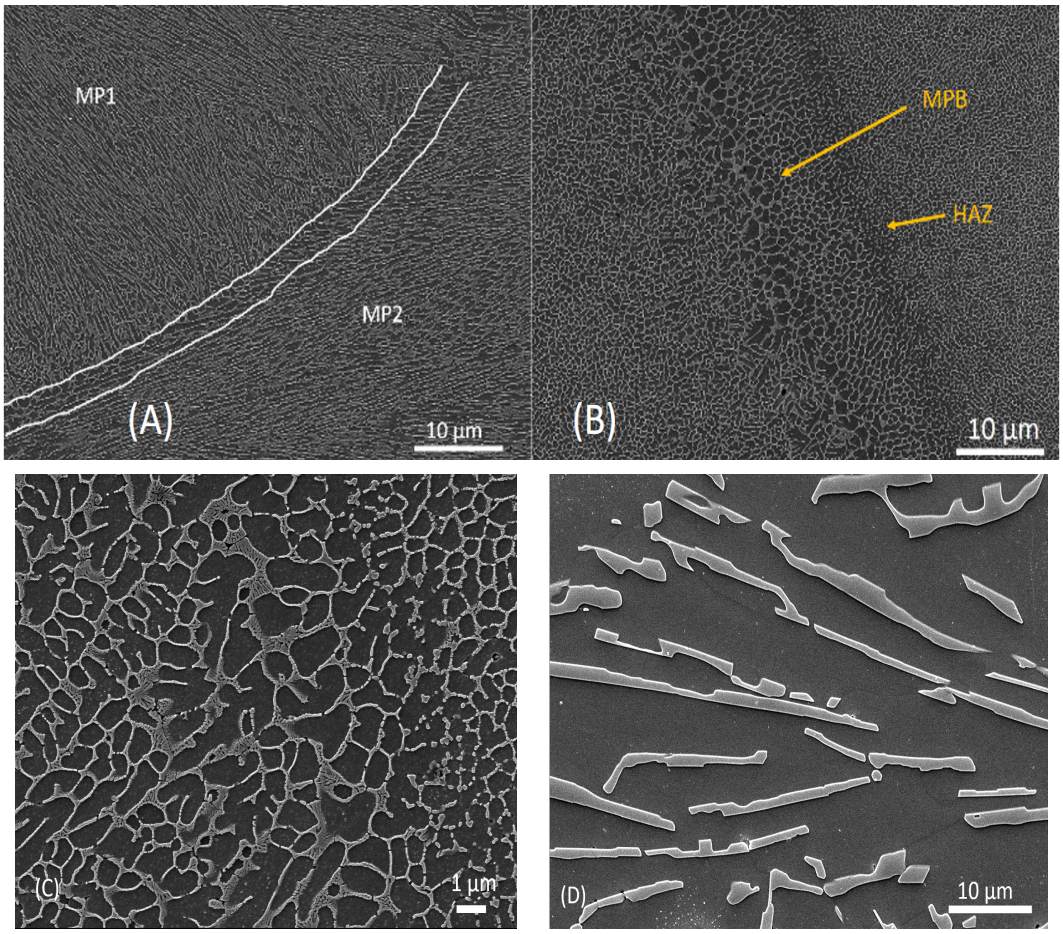

Figure 3.2: (A): FE-SEM image of an AMXZ samples, with: melt pool 1 (MP1), the melt pool contour enclosed between 2 white lines and melt pool 2 (MP2). (B): FE-SEM image of an AMXY samples, with MPB the melt pool border and HAZ the heat affected zone. (C): FE-SEM image of the eutectic phase in the melt pool border of an AMXY sample. (D): FE-SEM image of a CA sample. These samples were prepared with Keller's etchant.

Figure 3.2 (A) shows an image of an AMXZ sample, with MP1 a first melt pool, MP2 a second melt pool and the melt pool border in between the two white lines.

The microstructure of these three sections has a fine cellular-dendritic structure. The grains of these three domains differ in size and aspect ratio.[8] The microstructure of the AM parts has characteristic larger grains in the melt pool borders than in the bulk of the melt pools.

Figure 3.2 (A) shows the fine microstructure in the bulk of the melt pool, with aluminium cells embedded in a fine silicon network. This microstructure shows no lamellar eutectic phase, as was also seen in literature.[39] Figure 3.2 (B) shows an image of an AMXY sample, with a melt pool border (MPB) and a heat affected zone (HAZ) indicated. Furthermore figure 3.2 (B) shows that in the HAZ the silicon network is being disrupted. Figure 3.2 (C) shows that the melt pool borders contain a lamellar eutectic phase. Figure 3.2 (D) shows an image of a CA sample which has a much coarser microstructure and silicon network compared to the AM material.

Discussion of the microstructure

The difference in microstructure between the bulk of the melt pools and the melt pool borders is because the movement of the heat source, namely the laser beam, causes great differences in thermal gradients and in growth rate of the grains, as was reported by Thijs et al.[35]. These thermal gradients and growth rates are largest in the centre of the scanning track and are the smallest at the edges of the laser beam. Thijs et al.[35] reported that thermal gradients even in the order of $10^6 \frac{K}{m}$ are possible. Since the solidification rate is lower in the melt pool borders compared to the bulk of the melt pools the aluminum cells are larger, the silicon network is coarser and the eutectic phase has enough time to form in these melt pool borders. Furthermore the aluminium cells in the melt pool borders are more pure since silicon has more time for solid state diffusion. However this is not the case in the bulk of the melt pools resulting in no or almost no eutectic phase in the bulk of the melt pools. In the HAZ the silicon network is disrupted because during the remelting of the solidified material the temperature will increase and the silicon will diffuse at a higher rate in the aluminium phase. This in turn results in the spheroidization and coarsening of the silicon particles, and thus creating the idiomorphic silicon particles showed in figure 3.2 (B), as was also seen in literature.[39] The difference in microstructure between the cast alloy material and the AM material is because of the much larger thermal gradients in the AM material compared to the cast alloy, which results in a coarser microstructure of the cast alloy.

3.2 Galvanostatic anodizing in sulphuric acid electrolyte solution

3.2.1 Anodizing potential versus time

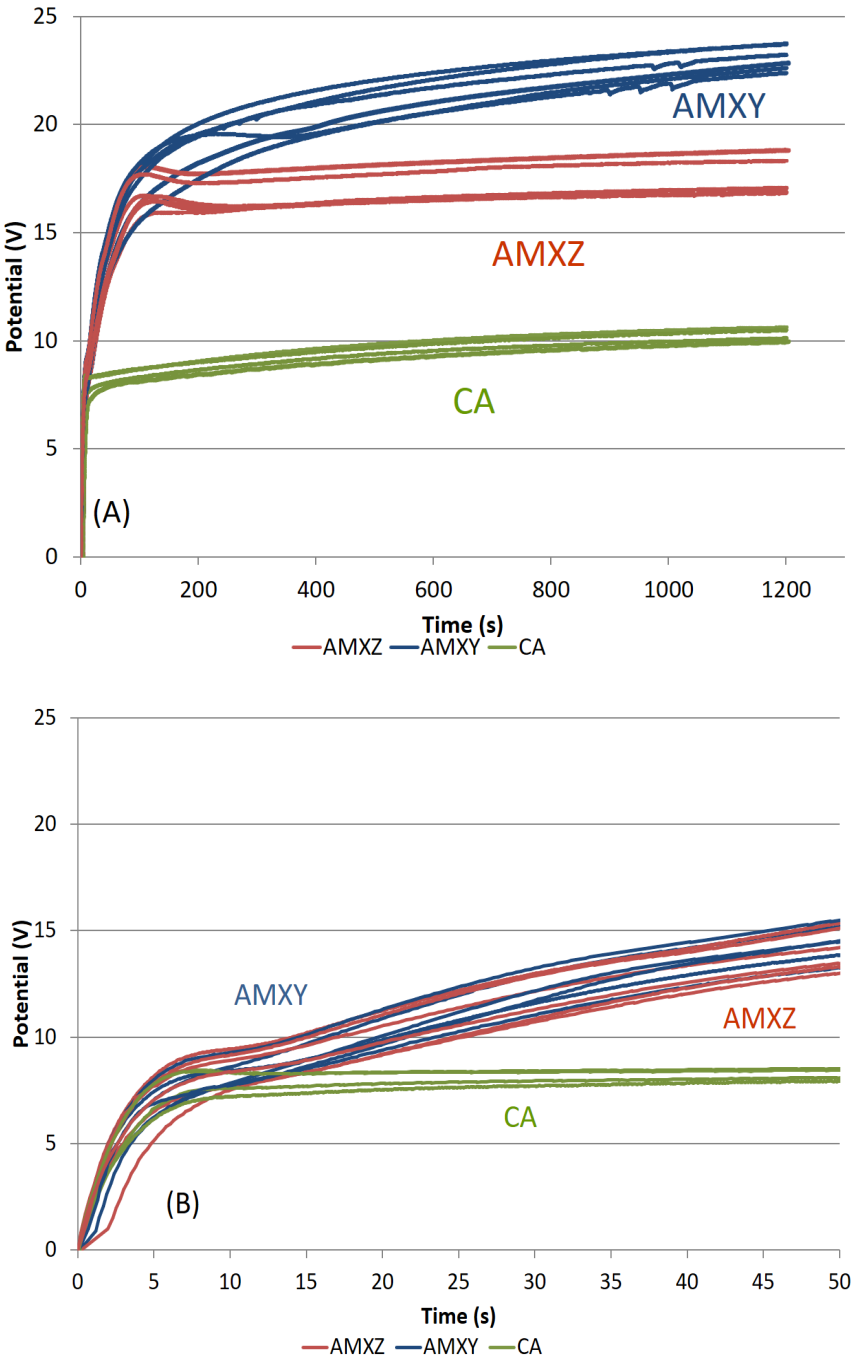

Figure 3.3: (A) Anodizing voltage-time evolution during galvanostatic anodizing of AM parts on the surface parallel to the building plane (AMXY) and to the building direction (AMXZ), and the anodizing of AA4420 cast alloy (CA) samples in a 3 M sulphuric acid solution at 25 °C with a current density of 10 mA/cm^2; (B) zoom into the first seconds of anodizing.

Figure 3.3 (A) shows the anodizing curves of AM parts, where the galvanostatic anodizing took place on the surface parallel to the building plane (AMXY) and to the building direction (AMXZ), and the anodizing of AA4420 cast alloy (CA) samples in a 3 M sulphuric acid solution at 25 °C with a current density of 10 mA/cm^2. The anodizing V-t curves of the cast alloy samples show a typical combined barrier/porous oxide growth behaviour.[17] The anodizing curves of the AM samples deviate from this typical behaviour. They show an initial rapid linear increase in potential, similar to the cast alloy sample, as can be seen in the zoom of figure 3.3 (B). But then after a few seconds of anodizing there is a change in slope, followed by a further increase to reach a higher steady state potential than for the cast alloy. Clearly however, the AMXY samples reach a higher potential in the steady state regime than the AMXZ samples and also the shape of the potential evolution is quite different; for the AMXZ samples the potential goes through a maximum before reaching a steady value, while for the AMXY samples the potential rise levels off more gradually not yet reaching a stable value after 1200 s.

3.2.2 Characterisation of the anodic oxide layer formed in sulphuric acid

3.2.2.1 Optical characterisation

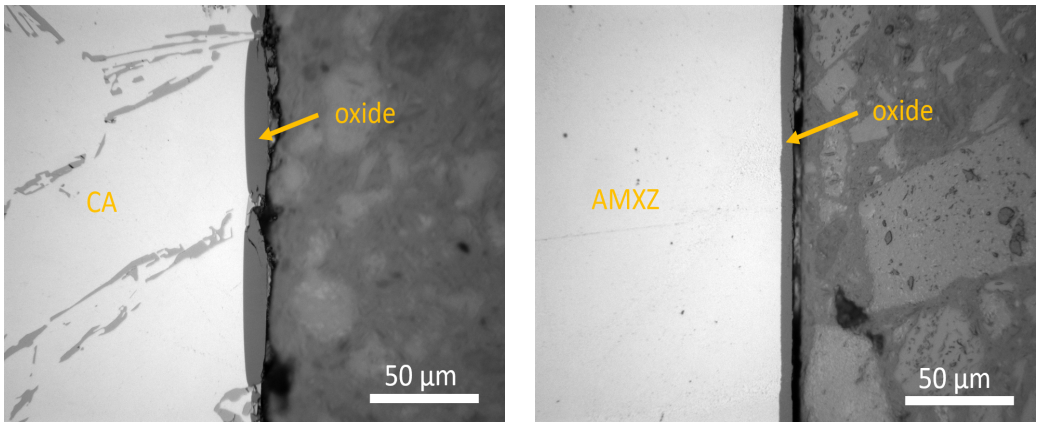

Figure 3.4: Optical microscopy images of the cross sections of an anodized AA4420 aluminium cast alloy sample (CA) and of an anodized AM part (AMXZ), with the anodized surface parallel to the building direction.

Figure 3.4 shows the optical microscopy images of the cross sections of an anodized AA4420 aluminium cast alloy sample (CA) and of an anodized AMXZ sample. The

anodizing was carried out galvanostatically in a 3 M of sulphuric acid solution, with a current density of 10 mA/cm^2 for 25 minutes. Figure 3.4 shows that the oxide film that is formed on the AM part is thinner and has a more homogeneous thickness distribution than for the cast alloy sample.

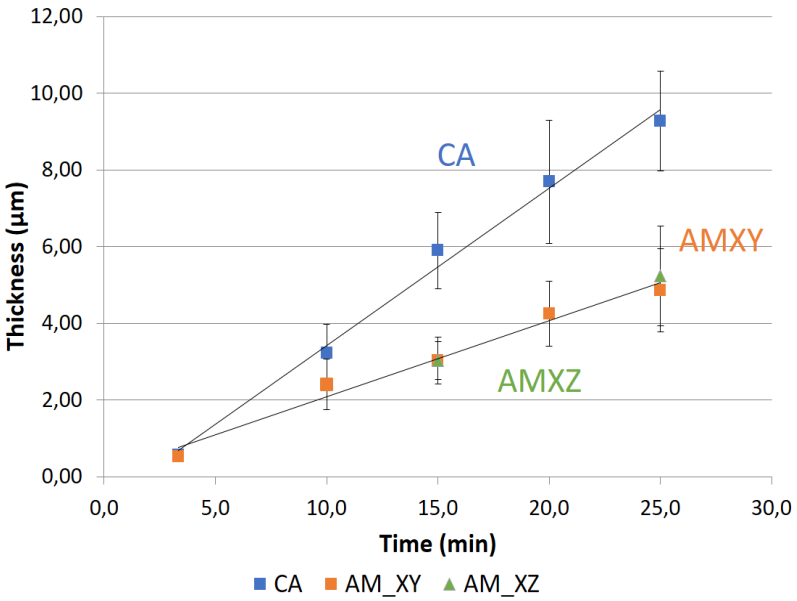

Figure 3.5: The thickness of the formed oxide layer as a function of the anodizing time for a AA4420 aluminium cast alloy (CA) and for an AM part, with the anodized surface being in the XY plane (AMXY) and in the XZ plane (AMXZ).

Figure 3.5 represents the thickness of the formed oxide layer -determined from OM images- as a function of anodizing time for AA4420 aluminium cast alloy (CA) and for AMXY and AMXZ samples. The anodizing was carried out galvanostatically in a 3 M of sulphuric acid solution, with a current density of 10 mA/cm^2 and this for various anodizing times. As can be seen the oxide formation appears to be linear for both the aluminium cast alloy as for the AM part, with the oxide film on the cast alloy growing faster than the oxide film on the AM samples. The oxide film of the cast alloy grows with a rate of 0.41 μm/min and the oxide film of the AM material grows with a lower rate of 0.2 μm/min.

3.2.2.2 SEM/EDX characterisation

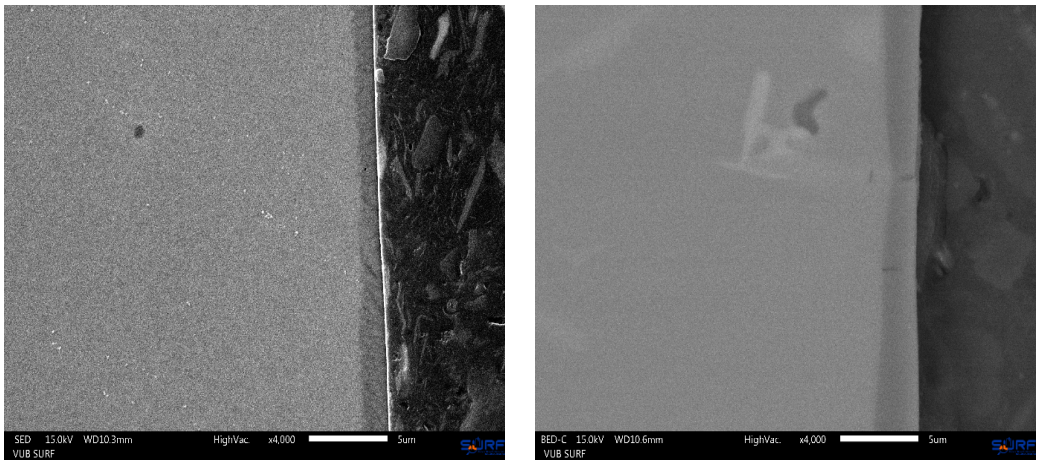

Figure 3.6: SEM images of the cross sections of: an anodized AMXY part (a) and an anodized AA4420 aluminium cast alloy sample.

Figure 3.6 represents the SEM images of the cross sections of: an anodized AMXY part (a) and an anodized AA4420 aluminium cast alloy sample. Both samples were anodized following the same anodization procedure. The samples were anodized galvanostatically in a 0.4 M sulphuric acid solution, for 18.7 minutes and with a current density of 5 mA/cm^2. It can be observed that the formed oxide layer for the AM part (a) is thinner and has a more homogeneous distribution of thickness compared to the formed oxide layer of the anodized AA4420 cast alloy. Corresponding EDX mappings are shown in figures 3.7 and 3.8.

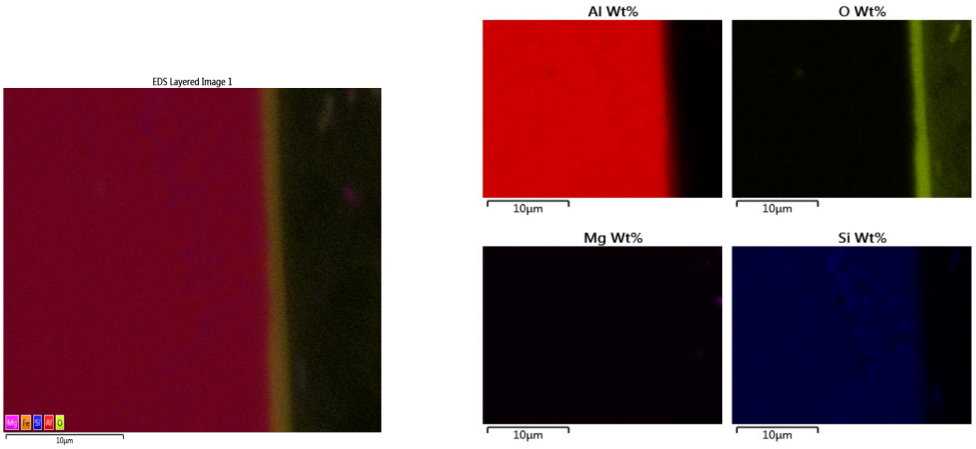

Figure 3.7: EDX elemental mapping of a cross section of an anodized AM part.

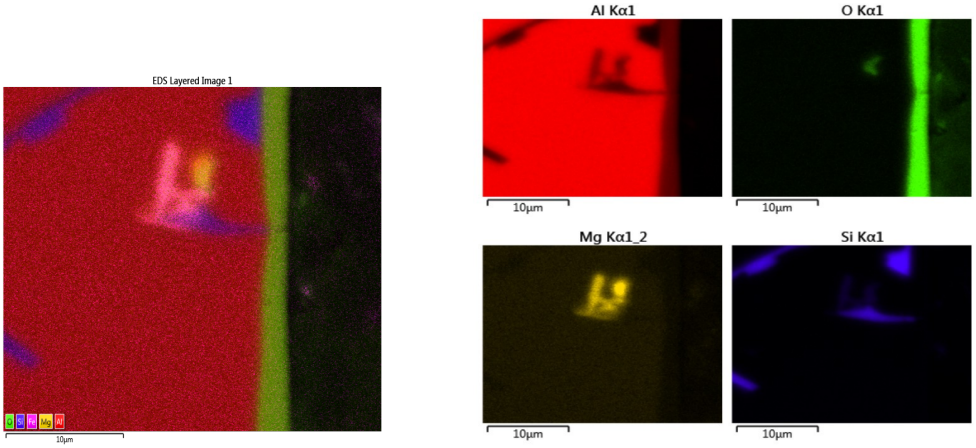

Figure 3.8: EDX elemental mapping of a cross section of anodized AA4420 aluminium cast alloy sample.

Figure 3.8 shows that the presence of a silicon particle causes the formed oxide layer to be locally thinner. This figure also shows that the formed oxide layer has a heterogeneous thickness distribution. Figure 3.7 on the other hand shows a more homogeneous distribution of the silicon network and also a thinner oxide layer with a more homogeneous thickness distribution.

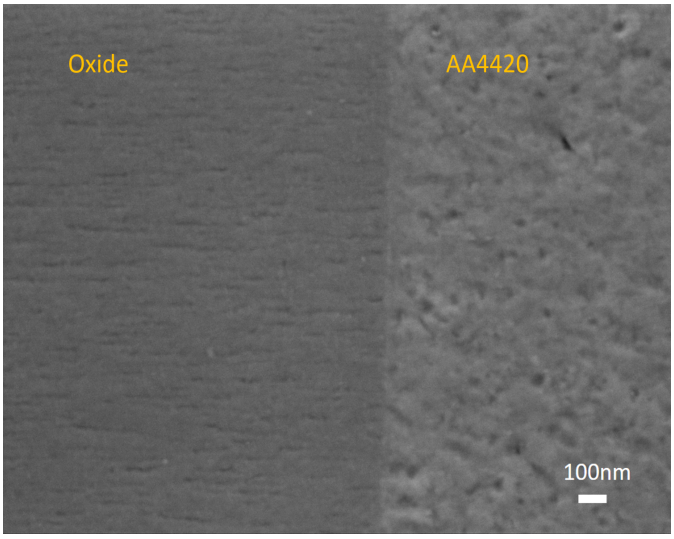

Figure 3.9: FE-SEM image of the pores in the formed oxide layer in the cast alloy AA4420.

Higher magnification FE-SEM images are shown in Figures 3.9, 3.10 and 3.11. Figure 3.9 shows the pores in the formed oxide layer on the AA4420 aluminium cast alloy. This image shows that all the pores in the oxide layer are oriented in the same direction, namely in the direction perpendicular to the moving oxide front, regressing into the substrate during anodizing. In figure 3.10 a region containing a silicon particle is shown. Clearly, when the oxide front encountered this silicon particle it changed direction and moved around the silicon particle, as reported also in literature.[27] In this way the oxide front faces the silicon particle and thus the formed pores are reoriented towards the silicon particle, as can be seen in the circle in the inset of figure 3.10.

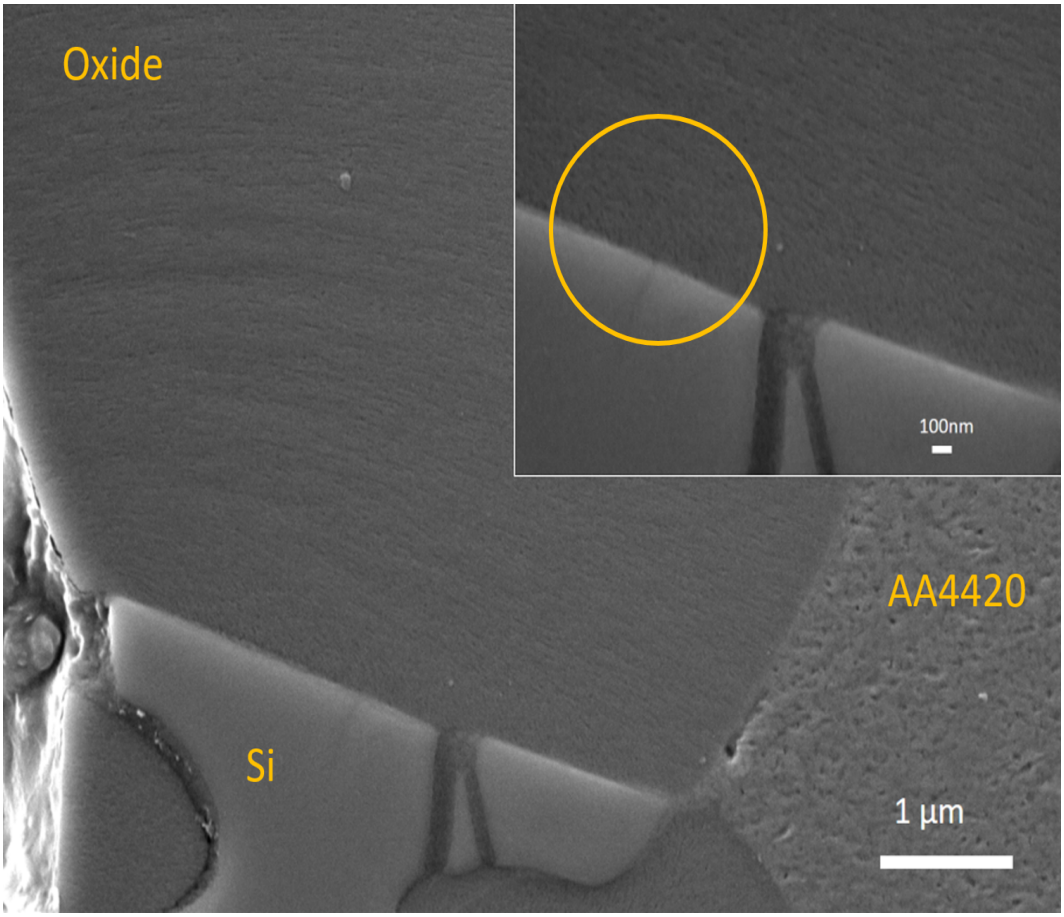

Figure 3.10: FE-SEM image of the oxide layer on the cast alloy AA4420.

Figure 3.11 shows the pores in the formed oxide layer on the AM material. For the AM material, both in the XY and XZ plane, the pores that are formed during anodizing in a 3 M sulphuric acid solution are not oriented in the same direction. They have an orientation following the fine distribution of the silicon network in the aluminium alloy.

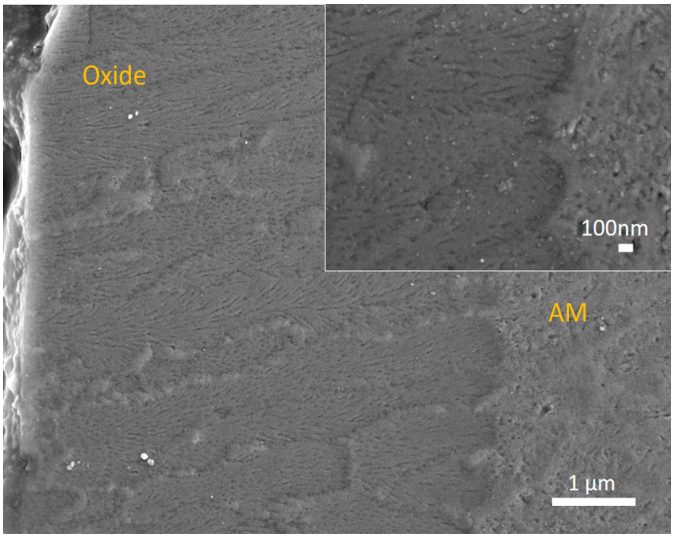

Figure 3.11: FE-SEM image of the pores in the formed oxide layer in the AM material.

In Figures 3.12 and 3.13 the outer surface of the anodized samples are shown after 3 and 30 sec of anodizing for the cast alloy and the AM alloy sample. In both cases pores are observed for the samples which were anodized for 3 and 30 seconds. The samples which were anodized for 3 seconds show only a few amount of pores, compared to the samples which were anodized for 30 seconds that show much more pores per surface area. These two figures further show that both the cast alloy and the AM alloy samples have about the same amount of pores per surface area after 3 and 30 seconds of anodizing.

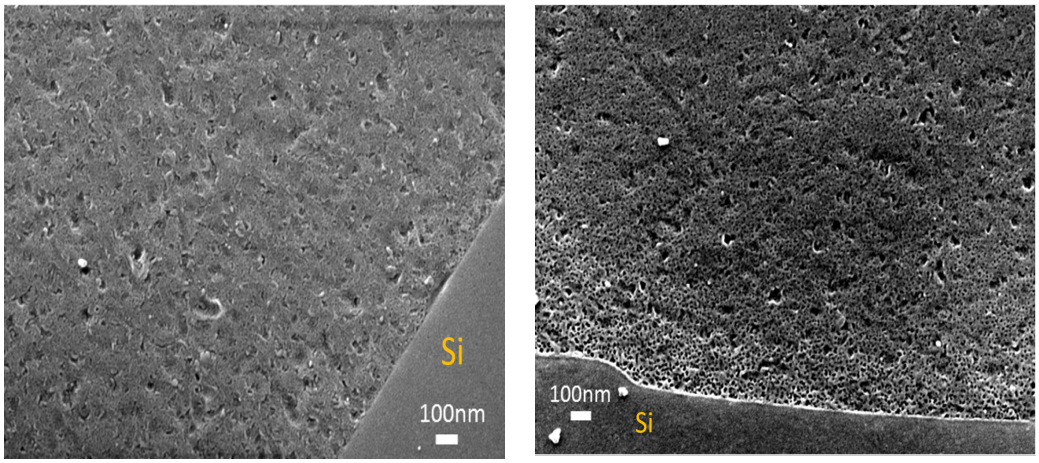

Figure 3.12: (left) FE-SEM image of the outer surface of the oxide layer in AA4420 cast alloy, after 3 seconds of galvanostatic anodizing in a 3 M sulphuric acid solution and (right) FE-SEM image of the outer surface of the oxide layer in AA4420 cast alloy, after 30 seconds of galvanostatic anodizing in a 3 M sulphuric acid solution.

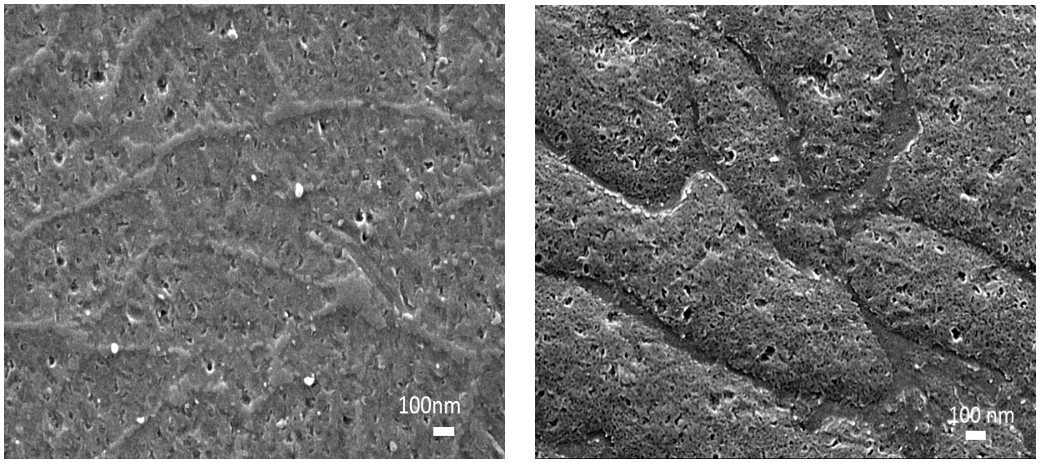

Figure 3.13: (left) FE-SEM image of the outer surface of the oxide layer in AM material, after 3 seconds of galvanostatic anodizing in a 3 M sulphuric acid solution and (right) FE-SEM image of the outer surface of the formed oxide layer in AM material, after 30 seconds of galvanostatic anodizing in a 3 M sulphuric acid solution.

3.2.2.3 AFM characterisation

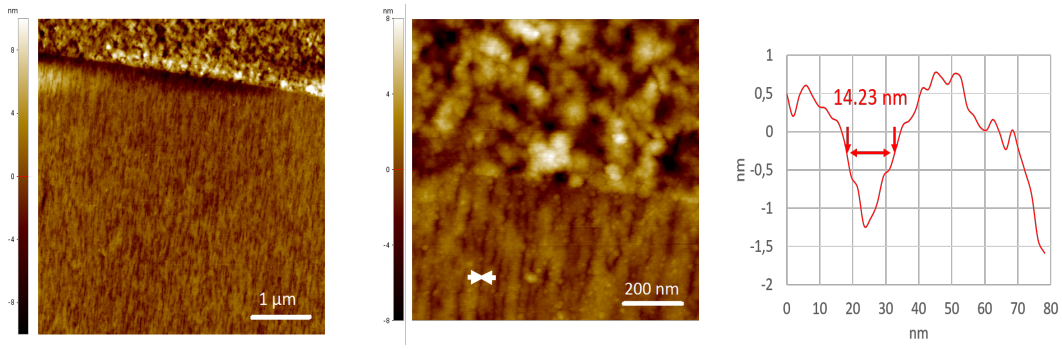

Figure 3.14: From left to right: AFM topography map of an area in the cross section of an anodized CA sample, detailed topography map of the same area and a topography profile of the line shown in the detailed topography map.

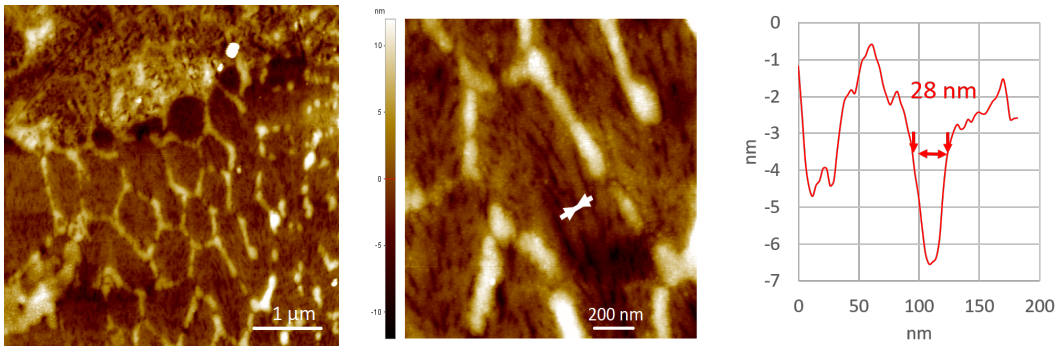

Figure 3.15: From left to right: AFM topography map of an area in the cross section of an anodized AM sample (AMXZ), detailed topography map of the same area and a topography profile of the line shown in the detailed topography map.

Figures 3.14 and 3.15 show AFM topography maps and line profiles of an area in the cross section of an anodized CA and AMXZ sample, respectively. The line profiles, shown in the detailed topography maps, cross a pore in the anodic oxide film. From this the pore diameter can be estimated. The average diameters of the pores, of the two samples, are calculated based on several line profiles and are listed in the table below.

	Pore diameter in nm	Predicted value of the pore diameter based on the steady state anodizing voltage (ratio 1.3 - 1.7 nm/V) in nm
CA	17.1 ± 3.6	13.5 - 17.7
AMXZ	24.4 ± 3.5	22.1 - 28.9

Table 3.1: The average pore diameter, calculated from AFM measurements, and the predicted value of the pore diameter based on the anodizing voltage-ratio, of an anodized AMXZ and CA sample.

The anodized AMXZ sample has experimentally a larger average pore diameter than the anodized CA sample. Further, when considering the pore dimensions that are predicted - according to literature - based on the anodizing voltage at steady state, i.e. pore diameter equals 1.3 - 1.7 nm/V, this difference is confirmed (see right column in table). Note that the experimentally determined average pore diameter is in the same range as the theoretical by literature predicted value for the average pore diameter.[40]

Discussion of the galvanostatic anodizing in sulphuric acid and of the anodic oxide layer

Figure 3.3 shows that for the cast alloy the anodizing potential time transient follows the behaviour reported in literature: first there is a rapid linear increase of the potential related in literature to the barrier formation, followed by a transition to a plateau value related in literature to steady state porous oxide growth, with the steady state potential value being proportional to the barrier layer thickness at the bottom of the porous section. For the AM samples the anodizing potential shows a different time evolution. The higher steady state potential or thus the higher electric field strength required for anodizing of the AM samples compared to the aluminium cast alloy samples can be explained by the fact that these AM samples have a much finer microstructure.[35] This fine microstructure of the AM samples is due to the high cooling rate[35] and expresses itself as a refined aluminium phase, a refined eutectic phase and a fine distribution of the silicon network. Literature reported that for aluminium-silicon cast alloys the silicon will obstruct the moving oxide front during anodizing.[27] This is because silicon will partially be anodized at a lower rate than aluminium.[27] Furthermore silicon is a semiconductor, unlike aluminium that is a conductor.[44] Because of the fine distribution of the silicon network in the AM material the oxide front will have a higher probability of encountering this silicon phase in the AM material compared to the CA material. Considering this higher probability together with the fact that the silicon network might be partially anodized and the fact that silicon is a semiconductor might explain the higher electric field strength required for anodizing of AM samples compared to CA

samples. This higher electric field strength can also be explained by the fact that the very high cooling rates in the AM material will cause for the aluminium cells to contain more silicon in solid state solution, compared to the cast alloy material which solidified with a much lower cooling rate. Since there is more silicon in the aluminium cells the probability of the oxide front encountering silicon is higher, this together with the fact that the silicon network might be partially anodized and the fact that silicon is a semiconductor might explain the higher electric field strength. Figure 3.3 (A) also shows that the AMXY samples have a higher electric field strength than the AMXZ samples, this can be explained by the difference in cooling rate in the bulk of a melt pool compared to the melt pool border. In the melt pool border the cooling rate is lower than in the bulk of melt pool and this results in a difference in microstructure, namely the microstructure in the bulk of the melt pool is finer. The microstructure in the bulk of the melt pool has a more refined aluminium phase, which contains more silicon in solid state solution, and a more homogeneously distributed silicon network. This means that the probability of the oxide front encountering silicon is lower in the melt pool border compared to the bulk of the melt pool. The microstructure of the bulk of the melt pool will thus obstruct the movement of the oxide front to a larger extend compared to the melt pool border. This means that in the bulk of the melt pool the electric field strength required for anodizing might be higher compared to a melt pool border because the probability of encountering silicon is higher in the bulk of the melt pool, and because silicon might partially anodize at a lower rate and because silicon is a semiconductor. And since the AMXZ samples contain in general more melt pool borders per surface area than the AMXY sample, the AMXZ samples will have in general a lower electric field strength required for anodizing. Figure 3.3 (A) also reports that there is a distribution of the required electric field strength for both the AMXY samples as for the AMXZ samples. This can be explained by the difference in surface state for all the additve manufactured samples, since the anodizing temperature, the electrolyte solution and the manufacturing process stays the same for all the samples. This difference in surface state is, to be more specific, a difference in amount of melt pool borders per surface area. So the distribution of required electric field strength for the AM samples can be explained by a distribution of the amount of melt pool borders per surface area in the AM samples.

Figure 3.3 shows a change in slope for the AA4420 cast alloy in the anodizing curve after a few seconds, according to literature this is the point where nucleation and growth of the pores start. This is confirmed by the FE-SEM images, taken after 3 and 30 seconds of galvanostatic anodizing in a 3 M sulphuric acid solution. After 3 seconds of anodizing only a few amount of pores per surface area are present in the oxide layer compared to the samples which were anodized for 30 seconds that show much more pores per surface area, which were initiated. Furthermore figures 3.12 and 3.13 show that both the cast alloy and the AM alloy samples have about the same amount of

pores per surface area after 3 and 30 seconds of anodizing.

The heterogeneous thickness distribution of the oxide layer of the cast alloy is caused by the silicon present in the alloy, that will obstruct the movement of the moving oxide front during anodizing.[27] As can be seen in figure 3.8 where the presence of a silicon particle causes for the required electric field strength to be locally higher and results in a locally thinner oxide film. On the other hand figure 3.7 shows a more homogeneous distribution of the silicon on the AM part. Thijs et al.[35] also reported this very fine distribution of the silicon phase in the AM parts. This fine and homogeneous distribution of the silicon network causes the required electric field strength to be higher not locally but almost over the entire anodizing surface resulting in a more homogeneous distribution of the oxide thickness.

In order to have a better understanding of the combined barrier/porous oxide growth behaviour, the barrier oxide growth behaviour was studied in this thesis. The results of this study is shown in the annex. However not enough research was done to have a good understanding of the barrier oxide growth behaviour and thus in the future more research should be done regarding this.

3.2.3 Evaluation of the corrosion resistance before and after anodizing

3.2.3.1 Open Circuit Potential

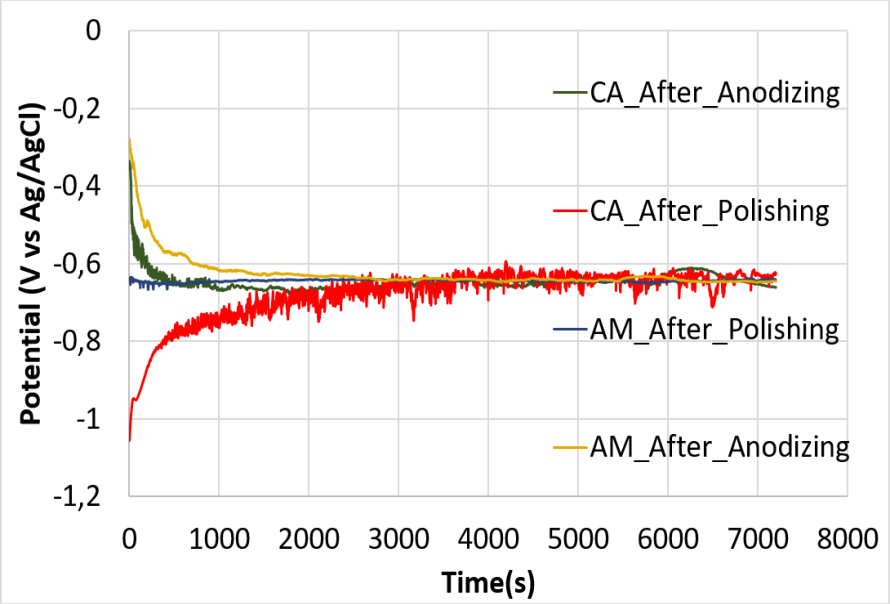

Figure 3.16: Open circuit potential as a function of immersion time in 0.1 M NaCl solution for AM samples (AM) and CA samples, after polishing and after polishing plus anodizing.

Figure 3.16 shows the open circuit potential (OCP) that is measured as a function of time for: polished AM samples, both AMXZ and AMXY, polished CA samples, galvanostatically anodized AM samples, both AMXZ and AMXY, and CA samples.

For the AM polished sample (blue curve) the OCP value remains more or less steady at about -0.65 V (vs the Ag/AgCl). For the cast alloy sample (red curve) the OCP value starts from -0.9 V to -1.1 V (vs the Ag/AgCl) right after immersion and stabilises to about -0.65 V (vs the Ag/AgCl) and shows an erratic evolution, resembling metastable pitting as was reported by Revilla et al.[38]

For the anodized AM material samples the OCP value range starting from -0.25 V to -0.65 V (vs the Ag/AgCl) right after immersion to stabilise at about -0.66 V (vs the Ag/AgCl). For the anodized cast alloy the OCP values range starting from -0.25 V to -0.65 V (vs the Ag/AgCl) right after immersion to stabilise at about -0.73 V (vs the Ag/AgCl).

Furthermore it can be noticed from figure 3.16 that for all the samples the potential stabilises after about 30 minutes.

	CA (AP)	AM (AP)	CA (AA)	AM (AA)
Pitting potential (V) (vs Ag/AgCl)	-0.64	-0.65	-0.73	-0.66
Error (V) (vs Ag/AgCl)	0.01	0.01	0.07	0.02

Table 3.2: The pitting potential of the AM samples and CA samples, after polishing (AP) and after anodizing (AA).

Discussion of the OCP measurements

Figure 3.16 shows that the starting potential is higher for the AM samples in comparison to the cast alloy samples. This might indicate that the natural oxide layer in the AM material is more noble and thus more protective than the natural oxide layer of the cast alloy. The cast alloy samples show a metastable pitting behaviour, which means that there is a continuous breakdown and repassivation of the oxide film. On the other hand the AM samples do not show this metastable pitting behaviour and show very stable values for the potential as a function of time, even immediately after immersion in the NaCl electrolyte solution. This is another indication that the natural oxide film of the AM material samples might be more stable than the oxide film, formed after polishing, on the cast alloy samples.

Figure 3.16 furthermore shows that the starting potential is about the same for the AM samples and the cast alloy samples. Figure 3.16 shows that the anodized cast alloy samples do not show a metastable pitting behaviour, but show a more stable behaviour as do the AM material samples. This indicates that the anodic oxide film of the AM material samples and of the cast alloy samples is more stable than the naturally formed oxide film.

It should be noted that the experiments were done in aerated solutions, this means that the corrosion potential is pinned down at the pitting potential.[38] The pitting potential for all the samples are shown in table 3.2. This table reports that the pitting potential value is about the same value for all of the samples, namely -0.65 V. Although the microstructures of the AM samples are very different from the cast alloy samples. This behaviour can be explained by the fact that the value of the pitting potential will result from a macroscopic material response rather than from a local material response, and because of the approximately same chemical composition of the cast alloy and AM material.[38]

3.2.3.2 Anodic polarisation

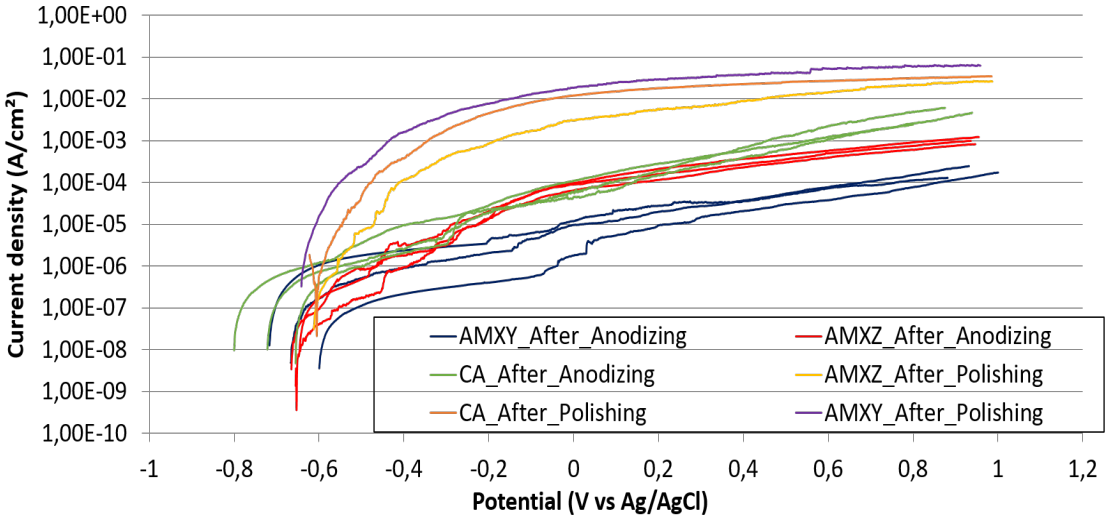

Figure 3.17: Representative anodic polarisation curves for the AM samples and the CA samples, after polishing and anodizing, in a 0.1 M NaCl solution and with a scanning rate of 0.1 V/min.

Figure 3.17 shows the anodic polarisation curves for AM samples and for cast alloy samples. This figure reports an in general large increase in current with increasing potential, this characterizes the pitting potential of the samples. The pitting potential of all the samples seem to be around -0.65 V (vs Ag/AgCl), which corresponds with the observed OCP data. Figure 3.17 shows that the polished samples (yellow, orange and purple curves) show a typical active behaviour. The cast alloy polished sample and the AM polished samples have very similar values and no distinct difference can be observed between them. Figure 3.17 shows that the anodized samples (red, blue and green curves) show a typical passive behaviour. This figure furthermore shows that the slope of this passive region is slightly larger in case of the anodized CA samples (green curves) compared to the anodized AM samples (red and blue curves).

It seems that for the anodized AM samples the AMXY samples (blue curves) have in general a slightly higher resistance against anodic polarisation compared to the AMXZ samples (red curves). Nevertheless in the polished samples this trend is not noticed, since the curves of the polished samples are very close to each other.

Discussion of the anodic polarisation measurements

These anodic polarisation measurements give a first indication of the corrosion properties of the samples. Figure 3.17 shows that the anodized samples have a better anodic polarisation resistance than the polished samples, this is because of the thicker anodic oxide film. The higher passivity of the anodized AM samples compared to the anodized CA samples could be explained by the fact that the pore orientation in the AM samples is much more variable compared to the CA samples, as was seen in figure 3.11. This variable orientation of the pores could obstruct the penetration of electrolyte in the anodic oxide film to a larger extend, thus resulting in a better protection against anodic polarisation.

The seemingly higher resistance against anodic polarisation of the anodized AMXY samples compared to the anodized AMXZ samples is also reported by Cabrini et al.[1]. They preformed electrochemical impedance spectroscopy and found that the absolute value of the impedance is lower at low frequencies immediately after immersion into the solution for AMXZ samples compared to AMXY samples. They suggest that this is because of the higher amount of melt pool borders per surface area for the AMXZ samples and also due to the difference in surface porosity density in the two AM samples.[1] This theory is furthermore strengthened by Revilla et al.[38], because they notice preferential corrosion attacks in the melt pool borders, thus strengthening the theory that the AMXZ samples are less resistant against anodic polarisation and are less corrosion resistant than the AMXY samples. However as can be seen in figure 3.17 the curves of the polished samples are very close to each other. This suggests that in general the AMXY samples have a higher anodic polarisation resistance than the AMXZ samples. But that there is a high dependence on the surface state and that the distribution in surface states of the samples causes a distribution in the obtained anodic polarisation curves.

Conclusion

SEM measurements reported that the AM material has a very fine microstructure, finer than the AA4420 cast alloy. This fine microstructure expresses itself as very small grain sizes, a fine eutectic phase and a fine and homogeneous distribution of the silicon network. This fine microstructure will have a large effect on the anodizing behaviour of this material. So was it noticed that in the galvanostatic anodizing process, in a sulphuric acid solution, the steady state potential of this AM material reached a higher value compared to the cast alloy that was anodized via the same process. During anodizing the oxide front has a higher probability of encountering silicon, which obstruct the movement of the oxide front, in case of the AM material. This higher electric field strength for the AM material might result from the fact that silicon might be partially anodized, at a lower rate, and because silicon is a semiconductor, unlike aluminium which is a conductor.

Furthermore despite the fact that there is a distribution of the amount of melt pool borders per surface area in the two AM samples, in general there are more melt pool borders per surface area in the AMXZ samples compared to the AMXY samples. These melt pool borders have a larger microstructure than the bulk of the melt pools, which expresses itself as larger aluminium cells, a coarser silicon network and an eutectic phase. The oxide front will have a smaller probability of encountering silicon in this coarser microstructure and thus the oxide front will be less obstructed in this microstructure. The bulk of the melt pool might then have a higher electric field strength compared to a melt pool border because of the higher probability of encountering silicon together with the fact that silicon might be partially anodized at a lower rate and because silicon in a semiconductor. This could explain why the AMXZ samples have a lower electric field strength.

Otical microscopy and SEM/EDX showed that the difference in microstructure between the AM samples and the CA samples also has an effect on the combined barrier/porous oxide growth behaviour. The AM samples have a lower porous oxide formation rate than the CA samples, more specific the oxide of the CA samples forms at a rate of 0.41 μm/min and the oxide of the AM samples at a rate of 0.20 μm/min. However the

formed oxide film of the AM samples has a more homogeneous thickness distribution compared to the CA samples. This is because of the fine distribution of silicon in the AM material that will cause an increase in electric field strength required for anodizing almost over the entire anodizing surface.

FE-SEM showed that the pores formed in the anodic oxide layer are in general oriented in the same direction for the CA samples, namely in the direction perpendicular to the moving oxide front. However when a silicon particle is encountered by the oxide front it will change direction and as a result the formed pores also will change orientation towards this silicon particle. The silicon network in the AM material is finer and more homogeneously distributed, as a result the formed pores will have a more variable orientation. Further FE-SEM also showed that the pores of the AM samples and the CA samples are formed at the same time during anodizing. From AFM measurements it can be concluded that the formed pores in the CA have a diameter of about 17.1 nm, and in case of the AM material the diameter of the pores is bigger. For example in case of the AMXZ samples the pores will have a diameter of about 24.4 nm. These values correspond to the in literature predicted values.

OCP measurements showed that all the anodized samples have approximately the same pitting potential at about -0.65 V. The anodic polarisation measurements showed that the anodized samples have an improved anodic polarisation resistance compared to the polished samples. The anodic polarisation measurements also showed a slightly higher anodic polarisation resistance of the AM samples compared to the CA samples. Which might be explained by the more variable orientation of the formed pores in the AM material that will prevent the impregnation of the electrolyte to a higher extend. Furthermore these measurements also showed an in general higher anodic polarisation resistance of the AMXY samples compared to the AMXZ samples. Which might result from the fact that AMXZ samples contain more melt pool borders per surface area compared to the AMXY samples. Further these melt pool borders were proven in literature to be less corrosion resistant.

In order to better understand the combined barrier/porous oxide growth behaviour the barrier oxide growth behaviour was studied. For this galvanostatic anodizing in an ammonium tartrate electrolyte solution was performed. These measurements showed a higher barrier oxide growth rate for pure aluminium compared to the AM samples and the CA samples. Furthermore these measurements also reported multiple slope changes for the AM samples and the CA samples. These changes in slope were unfortunately not understood and thus more research is required in order to have a better understanding of the barrier oxide growth behaviour.

The implication of this study on industry is that in order to have an anodic oxide film on the AM material with the same thickness and slightly improved corrosion properties

as the reference cast alloy material at least a double amount of energy is required for galvanostatic anodizing.

This thesis was able to give a better understanding of the combined barrier/porous oxide growth behaviour of the additive manufactured AlSi10Mg alloy in a sulphuric acid solution. By first studying the microstructure of this additive manufactured material, followed studying it's effect on the galvanostatic anodizing curves (anodizing potential in function of anodizing time) and the formed anodic oxide layer. The barrier oxide growth behaviour measurements were not able to give a good understanding of the mechanism and thus more research on this is needed. Furthermore the characterisation of the formed oxide is incomplete since the barrier oxide thickness was not determined. In future research TEM measurements will be done to characterise this barrier oxide thickness.

Annex

Galvanostatic anodizing in ammonium tartrate electrolyte solution

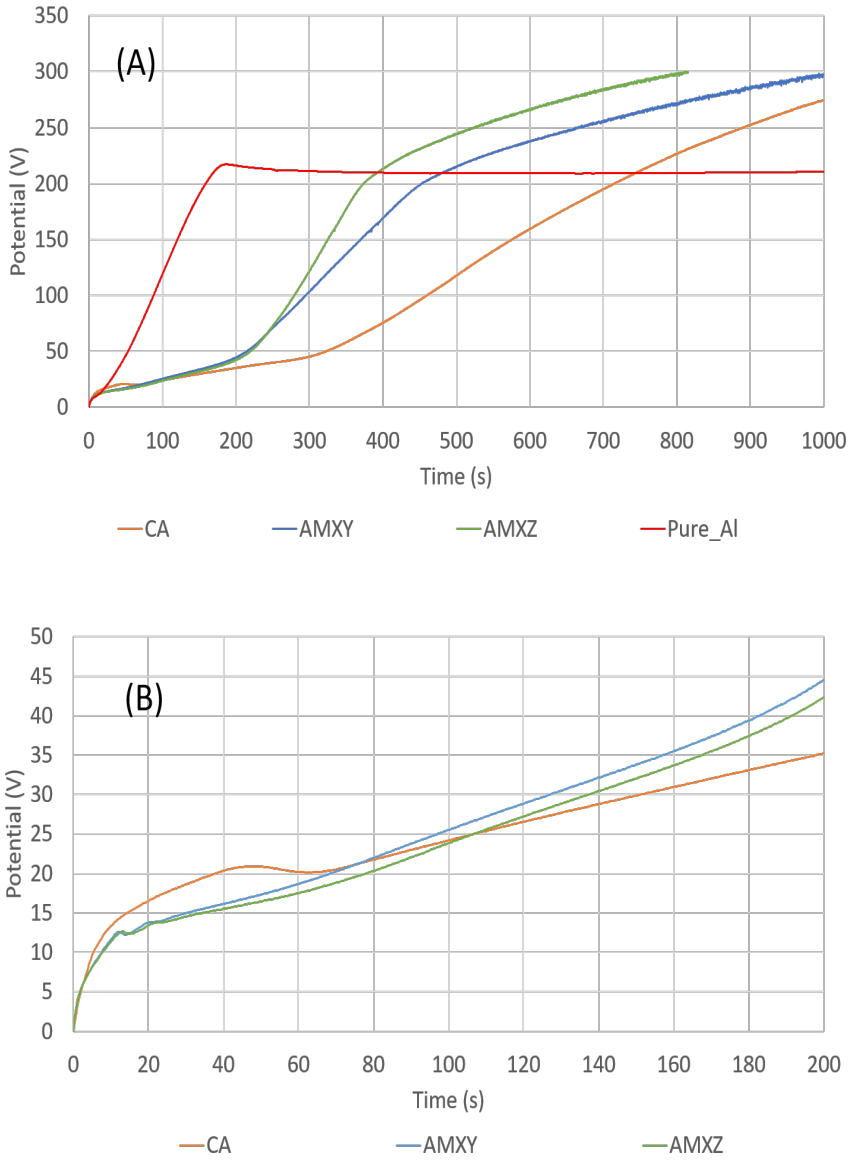

Figure 3.18: galvanostatic anodizing of: two AM samples AMXY and AMXZ, a pure aluminium (99.5 wt% Al) sample, and of a CA sample in a 0.15 M ammonium tartrate solution, at 25 °C and with a current density of 5 mA/cm^2; (A) represents the recorded anodizing potential as a function of time and (B) shows an enlarged section of the beginning of graph (A).

Figure 3.18 (A) shows the anodizing potential as a function of the anodizing time for: the AM samples (AMXY and AMXZ), a pure aluminium (99.5 wt% Al) and for a cast alloy sample. The anodizing of these samples was done in a galvanostatical way in a 0.15 M ammonium tartrate solution at 25 °C and with a current density of 5 mA/cm^2. Figure 3.18 (B) shows a detailed image of the beginning of the anodizing curves of figure 3.18 (A). The pure aluminium sample (red curve) shows a typical barrier oxide growth with the steepest slope. The AM samples (blue and green curves) and the CA sample (orange curve) show multiple changes in slope that are not shown by the pure aluminium sample. The first change in slope for the AM samples and the CA sample is shown in figure 3.18 (B) to be between 10 - 15 V. This decrease in slope indicates a reduction in resistance against anodizing. The second change in slope for the AM samples and the CA sample occurs at about 50 V, this increase in slope indicates an increase in resistance against anodizing. As can be seen in figure 3.18 (A) the AM samples show an extra change in slope, this decrease in slope occurs at about 200 V. Further it can be noticed that the slope of the AM samples is always larger than the CA sample.

Discussion

To have a better understanding of the combined barrier/porous oxide growth behaviour the barrier oxide growth behaviour is studied. Figure 3.18 shows that the pure aluminium (99.5 wt% Al) has the biggest slope. This means that the pure aluminium will form a barrier oxide film at the highest rate, compared to the other samples. This could be explained by the difference in microstructure of the samples. The pure aluminium does not contain many alloying elements, like for instance silicon, like the AM samples and the CA sample that will obstruct the movement of the oxide front. This silicon might be anodized partially at a lower rate compared to the aluminium. Further silicon is a semiconductor unlike aluminium, which is a conductor.[44] As a result the electric field strength required for the anodizing of the AM and CA samples is higher than the one of pure aluminium. This higher electric field strength causes a lower barrier oxide formation rate and thus a reduction in the slope of the anodizing curves of the AM and CA samples.

The fact that the AM samples always have a larger slope than the CA sample might be explained by the difference in microstructure of the AM samples compared to the CA sample. The AM material has a much finer microstructure and a much finer distribution of the silicon network compared to the CA material. The oxide front will have a higher probability of encountering silicon in the AM material than in the CA material. Considering this together with the fact that silicon might be anodized partially at a lower rate than aluminium, and the fact that silicon is a semiconductor,

might explain the higher electric field strength of the AM samples compared to the CA sample.

The multiple changes in slope shown by the AM and CA samples might be induced by the silicon alloying element. The first decrease in slope or decrease in electric field strength might be because of a change in morphology of the formed barrier oxide layer. For instance a porous oxide layer might start to form at this point. The next change and increase in slope or increase in electric field strength might indicate the point where the silicon phase will start to anodize. The last decrease in slope or decrease in electric field strength of the AM samples might indicate the point where the anodic oxide film will have its dielectric breakdown. However these are just speculations and in order to have a better understanding of the barrier oxide formation in the AM and CA material more research is required. It would for example be interesting if the morphology of the barrier oxide film could be characterised at different anodizing times.

Bibliography

[1] M. Cabrini et al., Evaluation of corrosion resistance of Al–10Si–Mg alloy obtained by means of Direct Metal Laser Sintering, Journal of Materials Processing Technology 231 (2016) 326–335.

[2] M. Cabrini et al., Corrosion resistance of direct metal laser sintering AlSiMg alloy, Surf. Interface Anal., 48, 818–826 (2016).

[3] Shiomi, M., Osakada, K., Nakamura, K., et al., Residual stress within metallic model made by selective laser melting process, CIRP Ann.—Manuf. Technol. 53(1), 195–198 (2004).

[4] Merceis, P., Kruth, J.-P., Recent development in aluminium alloys for the automotive industry residual stresses in selective laser sintering and selectivelaser melting, Rapid Prototyp. J. 12 (5), 254–265 (2006).

[5] A. Liu, C. K. Chua, K. F. Leong, Properties of test coupons fabricated by selective laser melting, Key Eng. Mater., 447-448, 780–784 (2010).

[6] M. Cabrini, S. Lorenzi, T. Pastore, S. Pellegrini, P. Fino, S. Biaminio, C. Badini, D. Manfredi, Corrosion resistance of direct laser sintering AlSiMg alloy, Eurocorr, Pisa (2014).

[7] Manfredi, D., Cagliano, F., Ambrosio, E.P., Krishnan, M., Canali, R., Biamino, S.,Pavese, M., Atzeni, E., Iuliano, L., Fino, P., Badini, C., Direct metal laser sintering: an additive manufacturing technology ready to produce light weight structural parts for robotic applications, Metall. Ital. 105 (10), 15–24 (2013).

[8] Manfredi, D., Calignano, F., Manickavasagam, K., Canali, R., Ambrosio, E.P., Atzeni,E., From powders to dense metal parts: characterization of acommercial AlSiMg alloy processed through direct metal laser sintering, Materials 6, 856–869 (2013).

[9] Thijs, L., Kempen, K., Kruth, J.-P., Van Humbeeck, J., Fine-sructuredaluminium products with controllable texture by selective laser melting of pre-alloyed AlSi10Mg powder, Acta Mater. 61, 1809–1819 (2013).

[10] Olakanmi, E.O., Selective laser sintering/melting (SLS/SLM) of pure Al, Al–Mg,and Al–Si powders: effect of processing conditions and powder properties, J.Mater. Process. Technol. 213, 1387–1405 (2013).

[11] Read, N., W, Wang, Essa, K., Attallah, M.M., Selective laser melting ofAlSi10Mg alloy: process optimisation and mechanical properties development, Mater. Des. 65, 417–424 (2015).

[12] R. L. Twite, G. P. Bierwagen, Review of alternatives to chromate for corrosion protection of aluminum aerospace alloys, Prog. Org. Coat., 33(2), 91–100 (1998).

[13] EOS, Laser sintering system EOSINT M 280 for the production of tooling inserts, prototype parts and end products directly in metal (2013).

[14] M. Saenz de Miera et al. Modelling the anodizing behaviour of aluminium alloys in sulphuric acid through alloy analogues, Corrosion Science 50 3410–3415 (2008).

[15] G. Patermarakis, K. Moussoutzanis, Transformation of porous structure of anodic alumina films formed during galvanostatic anodising of aluminium, Journal of Electroanalytical Chemistry 659 176–190 (2011).

[16] J.M. Albella, I. Montero and J.M. Martinez-Duart, Electrochim. Acta 32 (1987) 255.

[17] M.A. Paez, T.M. Foong, C.T. NI, G.E. Thompson, K. Shimizu, H. Habazaki, P. Skeldon and G.C. Wood, Corros. Sci. 38 (1996) 59.

[18] H. Habazaki, K. Shimizu, P. Skeldon, G.E. Thompson, X. Zhou, J. De Leat and G.C. Wood, Corros. Sci. 39 (1997) 719.

[19] F. Brown and W.D. Mackintosh, J. Electrochem. Soc. 148 (2001) 1096.

[20] G.E. Thompson, Y. Xu, P. Skeldon, K. Shimizu, S.H. Han and G.C. Wood, Philos. Mag. B 55 (1987) 651.

[21] S.S. ABDEL REHIM, H.H. HASSAN and M.A. AMIN, Galvanostatic anodization of pure Al in some aqueous acid solutions Part I: Growth kinetics, composition and morphological structure of porous and barrier-type anodic alumina films, Journal of Applied Electrochemistry 32: 1257–1264 (2002).

[22] V.P. Parkhutik, V.T. Belov and M.A. Chernyckh, Electrochim. Acta 35 (1990) 961.

[23] G. Patermarakis and D. Tzouvelekis, Electrochim. Acta 39 (1991) 2419.

[24] J.P. O,Sullivan and G.C. Wood, Proc. R. Soc. Lond. A. 317 (1970) 511.

[25] A.R. Despic and V.P. Parkhutike, Electrochemistry of aluminium in aqueous solutions and physics of its anodic oxide, in J.O.'M. Bockris, B.E. Conway and R.M. White (Eds), 'Modern Aspects of Electrochemistry' Vol. 20 (Plenum Press, New York, 1989), p. 397.

[26] L.E. Fratila-Apachitei, F.D. Tichelaar, G.E. Thompson, H. Terryn, P. Skeldon, J. Duszczyk, et al., A transmission electron microscopy study of hard anodic oxide layers on AlSi(Cu) alloys, Electrochim. Acta 49 (2004) 3169–3177.

[27] Baiwei Zhu, Salem Seifeddine, Per O.Å. Persson, Anders E.W. Jarfors , Peter Leisner, Caterina Zanella, A study of formation and growth of the anodised surface layer on cast Al-Si alloys based on different analytical techniques, Elsevier, Materials and Design 101 (2016) 254–262.

[28] F. Riddar, S. Hogmark, Rudolphi Å. Kassman, Comparison of anodised aluminium surface from four fabrication methods, J. Mater. Process. Technol. 212 (2012) 2272–2281.

[29] C.M. Dinnis, A.K. Dahle, J.A. Taylor, Three-dimensional analysis of eutectic grains in hypoeutectic Al-Si alloys, Mater. Sci. Eng. A 392 (2005) 440–448.

[30] A.L. Dons, L. Pedersen, L. Arnberg, The origin of 'anomalous' microsegregation in Al– Si foundry alloys—modelling and experimental verification, Mater. Sci. Eng. A 271 (1999) 91–94.

[31] L. Pedersen, L. Arnberg, Anomalous microsegregation in Al–Si foundry alloys, Mater. Sci. Eng. A 241 (1998) 285–289.

[32] E. Sjölander, S. Seifeddine, Optimization of solution treatment of cast Al-7Si-0.3Mg and Al-8Si-3Cu-0.5Mg alloys, Metall. Mater. Trans. A 45 (2013) 1916–1927.

[33] Olakanmi, E.O.; Dalgarno, K.W.; Cochrane, R.F., Laser sintering of blended Al-Si powders, Rapid Prototyp. J., 18, 109–119 (2012).

[34] Olakanmi, E.O.; Dalgarno, K.W.; Cochrane, R.F., Densification mechanism and microstructural evolution in selective laser sintering of Al-12Si powders, J. Mater. Proc. Tech., 211, 113–121 (2011).

[35] Thijs, L., Kempen, K., Kruth, J.-P., Van Humbeeck, J., Fine-structured aluminium products with controllable texture by selective laser melting of pre-alloyed AlSi10Mg powder, Acta Mater. 61, 1809–1819 (2013).

[36] Gibson, I., Rosen, D.W., Strucker, B., Rapid prototyping to direct digital manufacturing, Springer, XXII, 459 p. (2010).

[37] Nesma T. Aboulkhair, Ian Maskery, Chris Tuck, Ian Ashcroft, Nicola M. Everitt, The microstructure and mechanical properties of selectively laser melted AlSi10Mg: The effect of a conventional T6-like heat treatment, Materials ScienceEngineering A667 (2016) 139–146.

[38] Reynier I. Revilla, Jingwen Liang, Stéphane Godet, Iris De Graeve, Local Corrosion Behavior of Additive Manufactured AlSiMg Alloy Assessed by SEM and SKPFM, Journal of The Electrochemical Society, 164 (2) C1-C9 (2017).

[39] Couturiaux Gaëlle, Influence of process parameters on microstructure – AlSi10Mg cubes, INNOVIRIS and 4MAT internal document (2017).

[40] Pinner R., Wernick S., The surface treatment and finishing of aluminium and its alloys, Volume 1, Robert Draper LTD, pg 338 (1972).

[41] Yap C. Y., Chua C. K., Dong Z. L., Liu Z. H., Zhang D. Q., State-of-the-Art Review on Selective Laser Melting of Non-Ferrous Metals, Proceedings of the 1st International Conference on Progress in Additive Manufacturing (Pro-AM 2014), 193-201.

[42] Baoqiang Cong, Jialuo Ding, Stewart Williams, Effect of arc mode in cold metal transfer process on porosity of additively manufactured Al-6.3%Cu alloy, Int J Adv Manuf Technol (2015) 76:1593–1606.

[43] K. Schmidtkea, F. Palm, A. Hawkinsb, C. Emmelmannc, Process and Mechanical Properties: Applicability of a Scandium modified Al-alloy for Laser Additive Manufacturing, Physics Procedia 12 (2011) 369–374.

[44] Xiaoge Gregory Zhang, Electrochemistry of Silicon and Its Oxide, Kluwer Academic/Plenum Publishers, pg 91 (2001).

[45] Jingwen Liang, Study of corrosion properties of AlSi10Mg alloy processed by Selective Laser Melting Method, Vrije Universiteit Brussel, Elsene (2016).

[46] Herman Terryn, Iris De Graeve, Marie-Paule Delplancke,Surface treatment: Processing and Analysis, VUB - ULB, Etterbeek (2016).

[47] ASM handbook, vol. 4. Materials Park, OH: ASM International (1991).

[48] Wei Pei, Wei Zhengying, Chen Zhen, Du Jun, He Yuyang, Li Junfeng, Zhou Yatong, The AlSi10Mg samples produced by selective laser melting: single track, densification, microstructure and mechanical behaviour, Applied Surface Science 408 (2017) 38–50.

[49] U. Tradowsky, J.White, R.M.Wardb, N. Readb, W. Reimers, M.M. Attallahb, Selective laser melting of AlSi10Mg: Influence of post-processing on the microstructural and tensile properties development, Materials and Design 105 (2016) 212–222.

[50] L. Hitzler, C. Janousch, J. Schanz, M. Merkel, F. Mack, A. Öchsner, Non-destructive evaluation of AlSi10Mg prismatic samples generated by selective laser melting: Influence of manufacturing conditions, Mat.-wiss. u. Werkstofftech. 2016, 47, No. 5–6.